A NUMERICAL STUDY OF SLANTWISE CONVECTION

BY

Jinhui Huang

A thesis submitted to the Faculty of Graduate Studies and Research in partial fulfillment of the requirements for the degree of Master of Science.

Department of Meteorology
McGill University
Montreal, Quebec

October 1991

ABSTRACT

A two-dimensional anelastic model is used to study slantwise convection. The initial atmosphere is specified to be statically, inertially and symmetrically stable for dry convection. By varying the distribution of environmental relative humidity, a moist basic state potentially stable for upright convection but unstable for slantwise convection was obtained. The conditional symmetric instability (CSI) is released by specifying an initial streamfunction impulse.

The results show a typical slantwise convective circulation. A cloudband extends along the updraft of the CSI circulation. An energy budget analysis shows that the main source of perturbation kinetic energy comes from the vertical shear of the basic state flow, although the buoyancy term is important during the initial onset stage. It is also found that the CSI circulation induces both upright convective unstable layers and horizontal inertial unstable layers.

Although the decay stage has already been reached at the end of simulation, a neutral state with zero moist potential vorticity was not achieved. Our results also show that a high vertical resolution is necessary for the simulation of moist symmetric instability.

RESUME

Dans cette recherche, un modèle anélastique est utilisé pour étudier la convection oblique. L'état initial de l'atmosphère est déterminé comme étant statiquement, inertiellement et symétriquement stable pour la convection non-humide. En variant la distribution initiale de l'humidité relative environnementale, un état de base humide potentiellement stable pour la convection verticale mais instable pour la convection oblique, a été obtenu. L'instabilité conditionnelle symétrique (ICS) est libérée lorsqu'une impulsion de la fonction de courant initiale est spécifiée.

Les résultats montrent une circulation convective oblique typique. Une bande de nuages s'étend le long du courant d'air ascendant de la circulation ICS. Une analyse du bilan énergétique montre que la principale source d'énergie cinétique de perturbation vient du cisaillement vertical dans la circulation de base, même si la contribution de la force de bouée est importante durant l'étape initiale du développement de la circulation. Les resultats démontrent aussi que la circulation ICS induit la formation de strates verticales convectives instables et de strates horizontales inertiellement instables.

Malgré que l'étape de dissipation est atteinte à la fin de la simulation, un état neutre avec tourbillon potentielle humide nulle n'a pas été obtenu. Nos résultats ont aussi démontré qu'une haute résolution verticale est nécessaire pour la simulation d'instabilité symétrique humide.

ACKNOWLEDGEMENTS

I would like to express my deep appreciation to Dr. M. K. Yau for his invaluable assistance and guidance during the period of this study and throughout the preparation of the thesis.

In addition I would like to thank Dr. G. W. Reuter for his assistance in modifying the model and his constructive suggestions and advices.

Thanks also go to Alan Schwartz for his fruitful and timely help in computer support, to Dr. J. Sheng and many other colleagues for their help through discussion and to Paul Vaillancourt for translating the ABSTRACT into French.

The financial support provided by ONR Grant No: N00014-87-G-0171 is gratefully acknowledged.

TABLE OF CONTENT

LIST OF FIGURES

LIST OF TABLES

CHAPTER 1

INTRODUCTION

1.1 Rainband, slantwise convection and (conditional) symmetric instability

Many observational studies (e.g. Browning et al. 1973; Hobbs et al. 1980, etc) have shown that precipitation regions in extratropical cyclones are frequently organized in bands with an axis approximately parallel to the front. The width of the bands ranges from a few kilometres to about one hundred kilometres depending on their location relative to the front. The length of the bands also varies considerably, but for most bands it is on the order of several hundred kilometres. In addition, rainbands often exist for 6 to 12 hours (Hane,1986).

Fig. 1.1 depicts a schematic of typical features of cloud and precipitation patterns observed in an extratropical cyclone. Because of their effects on the distribution of intense precipitation, the study of cloud bands and rainbands, including the mechanisms for their initiation and maintenance, have become one of the most interesting research topics in mesoscale meteorology.

The conditions of the atmosphere (stability, vertical wind shear, etc.) can vary from one part of an extratropical cyclone to another. Therefore different rainbands may result from different mechanisms. Although many theories have been proposed to explain the existence of these bands, among these are boundary (Ekman) layer instability, gravity waves, wave-CISK and differential advection with a preferred scale for convection, it is believed that at least for the wide cold-frontal rainband, conditional symmetric instability (CSI) is the most likely cause (see Parsons and Hobbs, 1983 for details).

CSI is a mesoscale instability which appears in a baroclinic atmosphere (a region with synoptic-scale vertical wind shear) when an air parcel moves in a slantwise ascent under the unstable balance of the restoring forces (pressure gradient, coriolis and buoyancy forces) in the presence of latent heat release.

Bennetts and Hoskins (1979) are among the first to suggest the possible importance of CSI in the formation of frontal rainbands. They pointed out that although the condition for (dry) symmetric instability (SI) is rarely satisfied in frontal regions (Eliassen and Kleinschmidt, 1957), the realization of CSI is quite possible in a saturated atmosphere. By comparing their theoretical results with observations of rainbands, they concluded that CSI can be a dominant formative mechanism for rainband.

The results of many observation studies lend support to the relation between rainbands and CSI (Bennetts and Sharp, 1982; Parsons and Hobbs, 1983; Seltzer et al., 1985; Byrd, 1989; Reuter and Yau, 1990). By flying an instrumented aircraft along absolute momentum (M) surfaces, Emanuel (1988) found that while the atmosphere was quite stable to moist vertical displacement, it was almost exactly neutral to slantwise ascent. He hypothesized that a slantwise convective adjustment was occurring on time scales that are small compared to those of baroclinic processes.

1.2 Brief review of theory

The most complete analysis of the classical theory of dry SI is due to Emanuel(1979). The theory of moist SI was developed by Bennetts and Hoskins(1979) and Emanuel(1983a,b).

(1) Classical theory of dry SI

To explain the basic idea of the SI, we generalize the parcel method which is usually used in the analysis of static stability and inertial stability (more details can be found in Rogers and Yau, 1989). The coordinates are chosen such that the x axis is perpendicular to the band (or the front) and the y direction is along the band (or the front, see Fig. 1.2). In Fig. 1.3, we suppose that an air parcel at A is at equilibrium with the dry environment. With the displacement of the parcel to position B, the total acceleration of the parcel is

$$\frac{d\vec{v}}{dt} \equiv \frac{d^2\Delta}{dt^2}\hat{s} = \frac{dw}{dt}\hat{k} - \frac{du}{dt}\hat{i} \tag{1.1}$$

where $\vec{v}$ is the parcel velocity; Δ is the displacement; $\hat{s}$ is a unit vector in the direction of displacement. The vertical component of the force balance is

$$\frac{dw}{dt} = F_B = g\frac{(T_p - T_a)}{T_a} \tag{1.2}$$

where F_B is the buoyancy force, T_p is the temperature of the parcel and T_a is the temperature of the ambient environment. By writing the parcel temperature and the ambient temperature at point B as

$$T_p = T_A + (\frac{dT}{dp})dp \tag{1.3}$$

$$T_a = T_A + [\frac{\partial T}{\partial x}\delta x + \frac{\partial T}{\partial z}\delta z] \tag{1.4}$$

where T_A is the temperature at point A, and δx, δz are the displacements in the x and z directions, Rogers and Yau (1989) showed that

$$F_B = -\frac{g}{\theta}[\frac{\partial\theta}{\partial x}\delta x + \frac{\partial\theta}{\partial z}\delta z] \tag{1.5}$$

In the horizontal direction, because the parcel is at equilibrium at A, the net horizontal restoring force F_H at B is given by the difference between the incremental changes in the Coriolis force F_{Hf} and the horizontal pressure gradient force F_{Hp} .

$$F_{Hf} = \delta(-fv) = -f\delta v = -f(fu\delta t) = -f^2\,\delta x \tag{1.6}$$

$$F_{Hp} = \delta(-\frac{1}{\rho}\frac{\partial p}{\partial x}) = -f(\frac{\partial v_g}{\partial x}\delta x + \frac{\partial v_g}{\partial z}\delta z) \tag{1.7}$$

By defining the absolute momentum as $M = v_g + fx$, where v_g is the geostrophic wind in the y direction, the x-momentum equation becomes

$$\begin{aligned}\frac{du}{dt} = F_H = F_{HF}+F_{HP} &= -f(f\delta x + \frac{\partial v_g}{\partial x}\delta x + \frac{\partial v_g}{\partial z}\delta z)\\ &= -f[\frac{\partial M}{\partial x}\delta x + \frac{\partial M}{\partial z}\delta z]\end{aligned} \tag{1.8}$$

By substituting (1.2), (1.5) and (1.8) into (1.1), we get

$$\begin{aligned}\frac{d^2\Delta}{dt^2} &= F_B Sin\beta - F_H Cos\beta\\ &= -\frac{g}{\theta}[\frac{\partial\theta}{\partial x}\delta x + \frac{\partial\theta}{\partial z}\delta z]Sin\beta\\ &\quad + f[\frac{\partial M}{\partial x}\delta x + \frac{\partial M}{\partial z}\delta z]Cos\beta\end{aligned} \tag{1.9}$$

where β is defined in Fig. 1.3. Eq. (1.9) is a basic equation for the study of slantwise convection. Two special cases are of interesting. First, with pure vertical motion ($\beta = 90°$), (1.9) becomes

$$\frac{d^2z}{dt^2} = -\frac{g}{\theta}\frac{\partial\theta}{\partial z}\delta z \tag{1.10}$$

(1.10) describes the static stability for vertical displacement and the unstable condition is $\partial\theta/\partial z < 0$. If the motion is purely horizontal ($\beta = 0°$), (1.9) reduces to

$$\frac{d^2x}{dt^2} = -f\frac{\partial M}{\partial x}\delta x = -f(\frac{\partial v_g}{\partial x} + f)\delta x \tag{1.11}$$

(1.11) describes the inertial stability and the unstable condition is $\partial M/\partial x < 0$.

The above discussion shows that inertial, static and symmetric instabilities are very closely related in a dynamical sense. Each may be thought of as resulting from an unstable distribution of body forces acting on a fluid. In the case of static instability, the responsible body forces are gravitational, while the body forces are centrifugal in the case of inertial instability. These two differ principally in direction, with gravity acting vertically and centrifugal force radially. Symmetric instability simply represents motion resulting from a combination of these forces; thus the motion is 'slantwise' (Emanuel, 1983b). For this reason, symmetric instability is also known as slantwise convective instability.

Emanuel (1983b) showed that the instability criterion can be obtained by moving the parcel along θ surfaces. Thus

$$\begin{aligned}\frac{d^2\Delta}{dt^2} &= f[\frac{\partial M}{\partial x}\delta x + \frac{\partial M}{\partial z}\delta z]Cos\beta \\ &= fCos\beta\frac{\partial M}{\partial z}\delta x(\frac{\frac{\partial M}{\partial x}}{\frac{\partial M}{\partial z}} + \frac{\delta z}{\delta x}) \\ &= fCos\beta(\frac{\partial v_g}{\partial z})\delta x[(\frac{\partial z}{\partial x})_\theta - (\frac{\partial z}{\partial x})_M]\end{aligned} \tag{1.12}$$

(1.12) yields the stability condition,

$$\left|\frac{\partial z}{\partial x}\right|_{\theta} \begin{matrix} < \\ = \\ > \end{matrix} \left|\frac{\partial z}{\partial x}\right|_{M}, \qquad \begin{matrix} \textit{STABLE} \\ \textit{NEUTRAL} \\ \textit{UNSTABLE} \end{matrix} \tag{1.13}$$

where $\left|\frac{\partial z}{\partial x}\right|_{\theta}$ and $\left|\frac{\partial z}{\partial x}\right|_{M}$ are slopes of θ and M surfaces, respectively.

(1.13) can be shown to be equivalent to the criterions given by Stone (1966), and Hoskins (1978), which are

$$\frac{\zeta}{f} Ri \begin{matrix} > \\ = \\ < \end{matrix} 1, \qquad \begin{matrix} \textit{STABLE} \\ \textit{NEUTRAL} \\ \textit{UNSTABLE} \end{matrix} \tag{1.14}$$

and

$$PV \begin{matrix} > \\ = \\ < \end{matrix} 0, \qquad \begin{matrix} \textit{STABLE} \\ \textit{NEUTRAL} \\ \textit{UNSTABLE} \end{matrix} \tag{1.15}$$

where, ζ ($= f + \partial v/\partial x$) is the absolute vorticity, Ri [$= (g/\theta)\,(\partial\theta/\partial z)\,/(\partial v/\partial z)^2$] the Richardson number and PV [$=(1/\rho_0)(\,(\partial M/\partial x)(\partial\theta/\partial z)-(\partial M/\partial z)(\partial\theta/\partial x)\,)$] the potential vorticity.

Now, let us examine the stability of the parcel in Fig. 1.3 more closely. We assume that the environment is inertially stable ($\partial M/\partial x > 0$) and statically stable ($\partial\theta/\partial z > 0$). For a dry, inviscid parcel, the conservation of M and θ means that the x and z accelerations of the parcel will be proportional to its M and θ surpluses. In Fig. 1.3, it is evident that if the air parcel is displaced within the shaded area, for example from A to B, its M and θ values will be respectively less than and greater than those of its environment and the parcel will continue to accelerate. The important point here is that a slanted displacement may be unstable in an atmosphere which is statically stable for vertical displacement and inertially stable for horizontal displacement.

The solution of the fully viscous, adiabatic and Boussinesq linear equations (Emanuel,1979) reveals that SI results in a series of 2-D slanted roll circulations with their axes along the vertical shear vector. The slope of the circulation is comparable to that of the isentropic surface and the horizontal wavelength of the rolls is determined primarily by the depth of the unstable domain and the slope of isentropic surfaces rather than by the diffusive properties of the fluid.

(2) SI in a saturated atmosphere

The criterion for symmetric instability in the dry air is rarely satisfied in frontal regions (Eliassen and Kleinschmidt, 1957). So, it is necessary to consider the possibility of conditional symmetric instability in a saturated atmosphere where the effective static stability is reduced.

Many of the theoretical results for SI in a saturated atmosphere can be obtained as an extension of that for dry symmetric instability. For example, by using θ_e, equivalent potential temperature, in place of θ, we can rewrite the stability criteria (Eqs. (1.13), (1.14) and (1.15)) as

$$\left|\frac{\partial z}{\partial x}\right|_{\theta_e} \begin{matrix} < \\ = \\ > \end{matrix} \left|\frac{\partial z}{\partial x}\right|_{M} , \quad \begin{matrix} \mathit{STABLE} \\ \mathit{NEUTRAL} \\ \mathit{UNSTABLE} \end{matrix} \tag{1.16}$$

$$\frac{\zeta}{f} Ri_{\theta e} \begin{matrix} > \\ = \\ < \end{matrix} 1, \quad \begin{matrix} \mathit{STABLE} \\ \mathit{NEUTRAL} \\ \mathit{UNSTABLE} \end{matrix} \tag{1.17}$$

$$PV_{\theta e} \begin{matrix} > \\ = \\ < \end{matrix} 0, \quad \begin{matrix} \mathit{STABLE} \\ \mathit{NEUTRAL} \\ \mathit{UNSTABLE} \end{matrix} \tag{1.18}$$

where $\left|\frac{\partial z}{\partial x}\right|_{\theta_e}$ and $\left|\frac{\partial z}{\partial x}\right|_{M}$ are the slopes of the θ_e and M surfaces, respectively. $Ri_{\theta e}$ and

$PV_{\theta e}$ are the equivalent Richardson number and the equivalent potential vorticity, respectively. They are defined as

$$Ri_{\theta_e} \equiv \frac{\frac{g}{\theta_e}\frac{\partial \theta_e}{\partial z}}{\left(\frac{\partial v}{\partial z}\right)^2} \qquad (1.19)$$

$$PV_{\theta_e} \equiv \frac{1}{\rho_0}\left(\frac{\partial M}{\partial x}\frac{\partial \theta_e}{\partial z} - \frac{\partial M}{\partial z}\frac{\partial \theta_e}{\partial x}\right) \qquad (1.20)$$

Bennetts and Hoskins (1979) also gives the form of the perturbation growth rate γ for a symmetrically unstable motion in a saturated atmosphere, as

$$\gamma^2 = -(\alpha+1)^{-1}(\alpha f \zeta_\theta + f \zeta_{\theta_w})$$

where ζ_θ and $\zeta_{\theta w}$ are the absolute vorticities on θ and θ_w (wet-bulb potential temperature) surfaces, respectively; $\alpha = (h_u L_l)/(h_l L_u) = O(1)$ is a function of the updraft depth(h_u), downdraft depth(h_l), horizontal length of updraft(L_u) and horizontal length of downdraft(L_l). They estimated that for midlatitude situations, SI in a saturated atmosphere may have a doubling time on the order of hours.

Following Saitoh and Tanaka (1987), a summary for the symmetric stability criteria for a dry and saturated atmosphere is given schematically in Fig. 1.4.

(3) Symmetric instability in a moist atmosphere

For a moist but unsaturated atmosphere, Emanuel (1983a,b) extended the usual parcel method to slantwise ascent along a surface of constant absolute momentum M. CSI exists when the adiabatic temperature of the parcel along the M surface exceeds that of its environment in the usual way. The Slantwise Convective Available Potential Energy (SCAPE) can be calculated using

$$SCAPE(z) = {}_{M}\int_{l}^{z} \frac{g}{\theta_{vo}} (\Delta\theta_{v}) dz \tag{1.21}$$

where the subscript M denotes that the parcel is displaced along an M surface; l represent the initial position of the parcel; θ_{vo} is a constant reference virtual potential temperature and $\Delta\theta_{v}$ is the difference between the virtual potential temperature of a reversibly lifted parcel and that of its environment.

1.3 Numerical modelling of SI

Several important numerical modelling studies of dry and moist symmetric instability can be found in the literature.

Thorpe and Rotunno (1989) studied the nonlinear evolution of dry SI. The experiment was designed to examine the ultimate fate of a region of the atmosphere which is initially unstable to SI. The study was motivated by the fact that regions of near neutrality to CSI can often be found in the atmosphere but the details as to how such a state is established is not known. Their results show that with a patch of negative PV air embedded initially in a larger domain with positive PV, the initial unstable region broke up into small subpatches with positive and negative PV after the unstable SI circulation has ceased. These subpatches persist with no sign of being removed. They suggested a diffusive scheme which diffuses PV downgradient to remove the negative PV.

Bennetts and Hoskins (1979) conducted a numerical simulation using a two-dimensional primitive equation model. Condensation in a saturated atmosphere is parameterized and they obtained a roll circulation associated with the release of CSI characterized by a strong concentrated slanting updraft and a weaker, broad returning downdraft. They noted the almost exponential growth of the maxima of the cross-band streamfunction and the perturbation velocity.

Another numerical experiment of CSI was carried out by Saitoh and Tanaka (1987,1988). The initial condition was unstable for CSI but stable for dry SI. Slantwise motion was initiated by the addition of a few percents of supersaturation at the centre of the domain, superimposed on a random vertical velocity field. They used grid lengths of $\Delta x = 2$ km,and $\Delta z = 500$ m and obtained a typical slantwise CSI circulation with a horizontal scale of about 150 km. The slantwise stratiform cloud extended along the updraft of the CSI circulation and a convectively unstable layer was found above the cloud. Convective cells appeared in this unstable layer resembling the generating cells in observed bands. They also found that an increase of low-level water vapour supply enhanced the upper level convective unstable layer resulting in more vigorous generating cells.

Using a two dimensional, hydrostatic, primitive equation model, Knight and Hobbs (1988) investigated CSI forced by frontogenesis and its role in producing rainbands near a cold front. In their simulation the banded structures formed in a convectively stable region. The bands formed and intensified in a region of CSI. The bands disappeared when equivalent potential vorticity was everywhere positive. They also found that many of the characteristics of the bands, such as the slope of the updrafts and the spacing of the bands, agree well with the theory of CSI. In particular, in the region of CSI, the vertical velocity in the bands increased exponentially with time, although the growth rate is smaller than that predicted by linear analysis. Horizontal resolution sensitivity experiments were also performed. The results showed that the strength and horizontal scale of the bands were about the same with $\Delta x = 5$ km and $\Delta x = 10$ km. But the bands were poorly resolved when $\Delta x = 40$ km and were completely absent with $\Delta x = 80$ km.

Recently, Persson and Warner (1991) presented a CSI simulation. The model used was also a two dimensional, hydrostatic primitive equation model. No convective parameterization was used, but saturation was allowed to occur on the grid scale. The resolution in their 'control' case was $\Delta x = 10$ km, $\Delta\sigma = -0.0133$ ($\Delta p = -11.3$ mb, 75 model layers). The initial conditions consisted of a broad, baroclinic zone with a constant south-north potential temperature gradient (-3.3 K (100 km)$^{-1}$). The moisture field was specified such that the relative humidity isohumes were concentric ellipses. A small velocity perturbation centred in the relative humidity maximum was used to initiate the convection. By adjusting the humidity and temperature fields, conditions were obtained that were potentially unstable to moist SI, but stable to dry SI and to upright convection. In the control case, they simulated the whole life cycle of the CSI circulation, from its growth stage to its decay. The numerical results showed many features predicted by linear theory. One of the main findings was that spurious gravity waves can be produced in a hydrostatic primitive equation simulation of CSI from the inconsistency in specifying the vertical and horizontal resolutions. To estimate the optimal vertical resolution, they suggested that the parameter $AS = (\Delta p/\Delta x)/s$ should have a value of one. Here Δp and Δx are the vertical and horizontal grid spacings, respectively, and s is the frontal slope.

1.4 Purpose of this research

The purpose of this research is to study the characteristics of the slantwise convection and the evolution of CSI using a two-dimensional anelastic model which has been used successfully in cloud modelling. More specifically, we first modified this model to include the v-momentum equation, the coriolis force and a new initialization scheme. Numerical experiments are then performed and the evolution of slantwise convection documented.

Particular attention will be paid to some important features such as the details of the time development of $PV_{\theta e}$, the perturbation kinetic energy budget, and the mechanism for the generation of the convective unstable layer by the CSI circulation.

In the following chapter, the key features of the model are summarized. The experiment and results are described and discussed in chapter 3. Finally, the summary and concluding remarks are given in chapter 4.

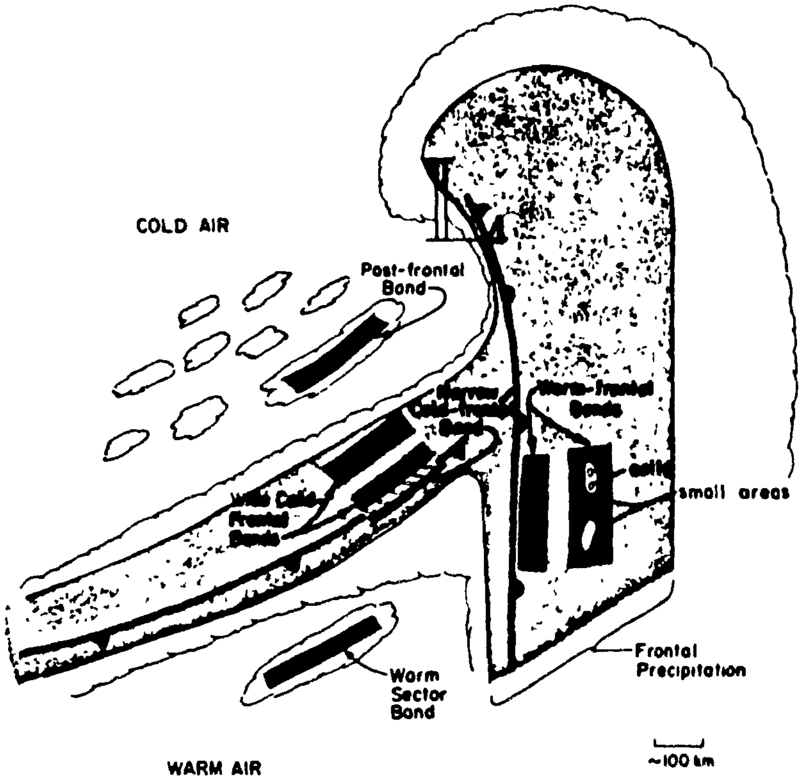

Fig. 1.1. Schematic of typical features of the cloud and precipitation pattern of an extratropical cyclone. Low pressure centre is indicated by L. Fronts are indicated by standard symbols. (After Houze, 1981)

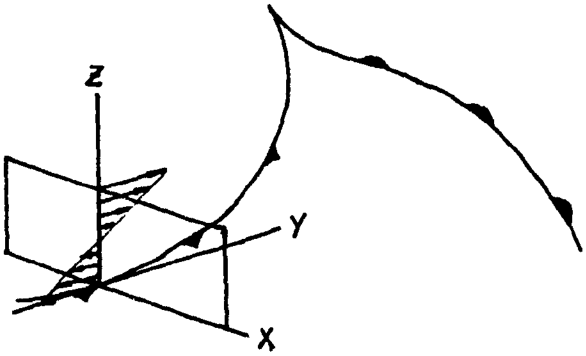

Fig. 1.2. The coordinate system. Directions of x, y and z coordinates are in the cross-frontal, along-frontal and vertical directions, respectively.

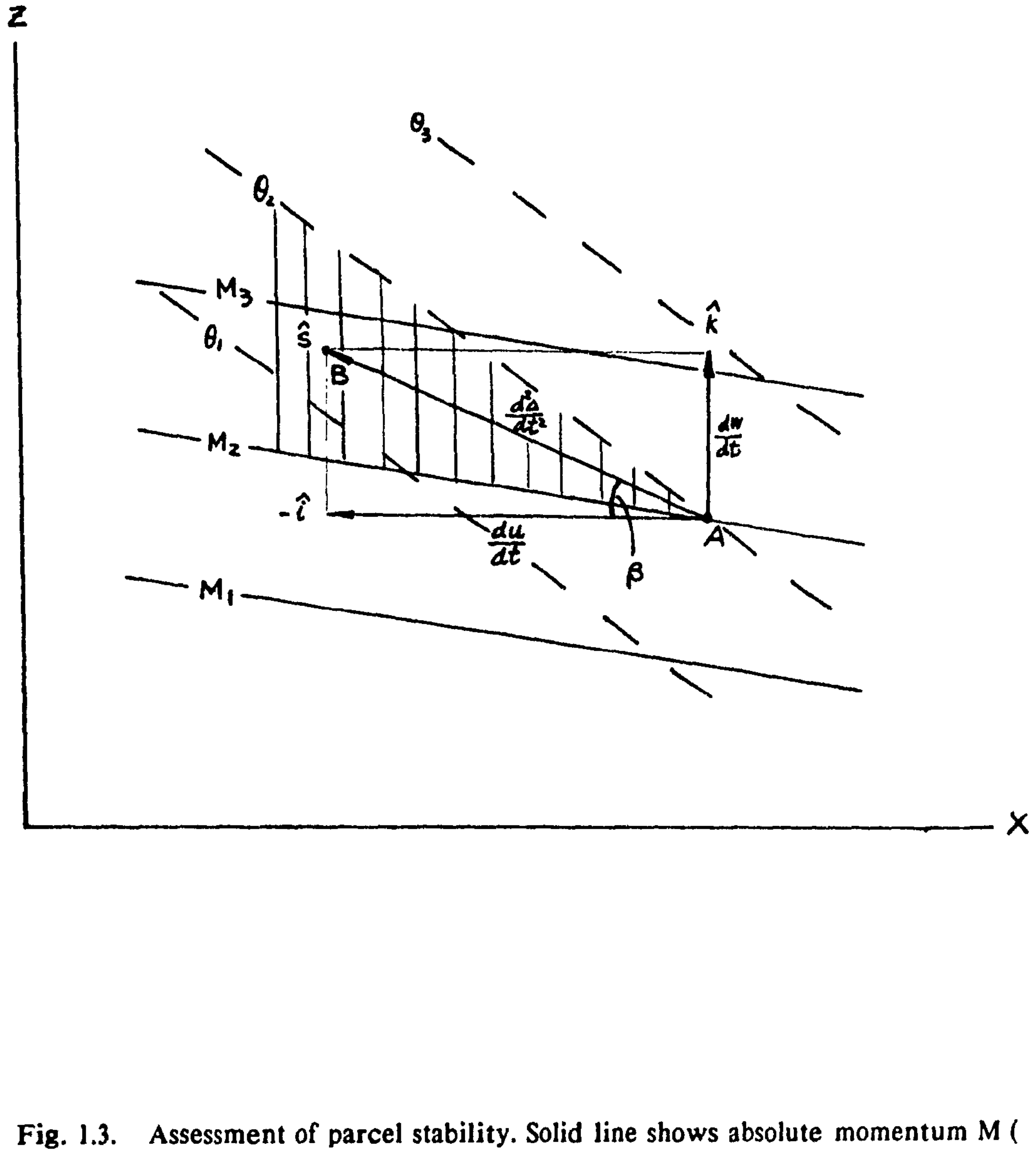

Fig. 1.3. Assessment of parcel stability. Solid line shows absolute momentum M ($= v_g + fx$), $M_1 < M_2 < M_3$; Dashed line shows potential temperature θ, $\theta_1 < \theta_2 < \theta_3$. $d^2\Delta/dt^2\ \hat{s}$ is the total acceleration vector while $dw/dt\ \hat{k}$ and $-du/dt\ \hat{i}$ are its two components. β is the angle between the direction of displacement and the x axis.

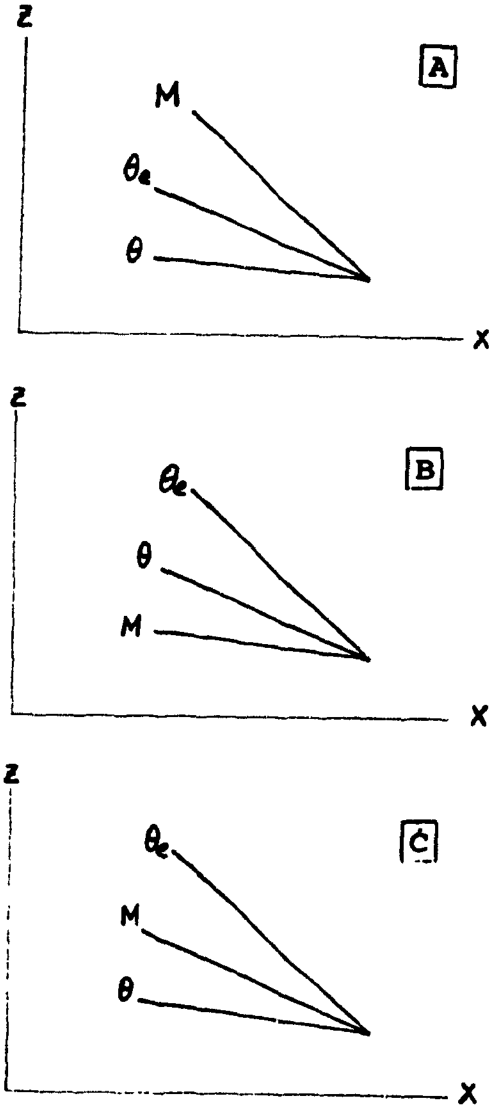

Fig. 1.4. Schematic figures which show the configurations of constant potential temperature, equivalent potential temperature and absolute momentum surfaces in the case of (A) stable to both SI and CSI; (B) unstable to both SI and CSI and (C) stable to SI but unstable to CSI. (Adopted from Saitoh and Tanaka (1987)).

CHAPTER 2

DESCRIPTION OF THE MODEL

The model used in this research is a slab-symmetric version of a cloud model developed by Steiner(1982) and subsequently modified by Reuter and Yau(1987a,b) and Hedley and Yau(1988). For the study of slantwise convection, coriolis force terms and the equation for v component of the velocity are added.

2.1 Basic assumptions

(1) Two Dimension Assumption. In extratropical cyclones, the basic thermal wind blows along the fronts. All physical variables are assumed uniform in the along-front direction ($\partial/\partial y = 0$). (see Fig. 1.2)

(2) Basic State. The basic state is assumed to be hydrostatic and geostrophic. No vertical and cross-band winds (i.e. $w_0 = 0$, $u_0 = 0$) are present in the basic state. The along-band wind v_0 is specified to have a constant vertical shear. It has negative values near the ground and positive values at the top (see Fig. 2.1 (A)). With this velocity field and a constant coriolis parameter, the surfaces of absolute momentum M appear to be straight lines in the cross-band section. To get a dry symmetrically stable state, we set the dry potential vorticity to 0.3 pvu (1 pvu $= 10^{-6}$ K m^2 kg^{-1} s^{-1}). As a result, the surfaces of potential temperature θ will also be straight lines in the cross band section and can be calculated in the manner shown in the Appendix. The resulting M and θ fields are shown in Fig. 2.1(B).

To obtain the initial pressure and temperature, we first use the equation for v_0, the hydrostatic and the geostrophic relations to calculate $\partial\pi/\partial x$ and $\partial\pi/\partial z$, where π is a dimensionless pressure function

$$\pi \equiv \left(\frac{P}{1000}\right)^{\frac{R_d}{c_{pd}}},$$

R_d is the gas constant for dry air and c_{pd} is the specific heat of dry air at constant pressure. Then by integrating the gradient of the dimensionless pressure horizontally and vertically, we get $\pi(x,z)$. The pressure field $P(x,z)$ can be obtained through the defining equation for π. The temperature field can be calculated using $T = \pi\,\theta$.

We shall specify the relative humidity profile in section 3.1 to arrive at a basic state which is potentially unstable for moist slantwise convection.

(3) Water substance. Water occurs only in the vapour and liquid phases. Condensation occurs whenever the water vapour mixing ratio exceeds the saturation value. Precipitation processes and ice physics are not included. Also, liquid water, in the form of cloud droplets, is assumed to move with the air.

2.2 Fundamental equations

(1) Deep anelastic continuity equation

The continuity equation for an anelastic slab-symmetric flow is

$$\frac{\partial u}{\partial x}+\frac{1}{\rho_o}\frac{\partial}{\partial z}(\rho_o w)=0 \tag{2.1}$$

where u and w are the x-component and z-component of velocity respectively, ρ is the air density and the subscript $_o$ refers to values in the basic state.

(2) Equations of motion

The equations are derived from Newton's second law of motion of the form

$$\frac{\partial u}{\partial t}+u\frac{\partial u}{\partial x}+v\frac{\partial u}{\partial y}+w\frac{\partial u}{\partial z}=-\frac{1}{\rho}\frac{\partial P}{\partial x}+fv+F_x \tag{2.2}$$

$$\frac{\partial v}{\partial t}+u\frac{\partial v}{\partial x}+v\frac{\partial v}{\partial y}+w\frac{\partial v}{\partial z}=-\frac{1}{\rho}\frac{\partial P}{\partial y}-fu+F_y \tag{2.3}$$

$$\frac{\partial w}{\partial t}+u\frac{\partial w}{\partial x}+v\frac{\partial w}{\partial y}+w\frac{\partial w}{\partial z}=-\frac{1}{\rho}\frac{\partial P}{\partial z}-g-gq_l+F_z \tag{2.4}$$

where q_l is the liquid water mixing ratio and F_x, F_y and F_z are the turbulence(friction) terms.

By writing the variable as the sum of a basic state portion (denoted by $_o$) and a perturbation portion (denoted by $'$), we get

$$A=A_o(x,z)+A'(x,z,t) \tag{2.5}$$

where A stands for u, v, w, T, P, etc. The perturbations are small and satisfy

$$\frac{P'}{P_o}<1,\quad \frac{\rho'}{\rho_o}<1,\quad \frac{T'}{T_o}<1 \tag{2.6}$$

so the first two terms on the right hand side of (2.4) can be simplified by neglecting the products of the perturbation quantities and using the hydrostatic assumption $\partial P_0/\partial z = -\rho_0 g$, Thus

$$\begin{aligned}-\frac{1}{\rho}\frac{\partial P}{\partial z}-g &= -\frac{1}{\rho_o(1+\frac{\rho'}{\rho_o})}\frac{\partial}{\partial z}(P_o+P')-g \\ &= -\frac{1}{\rho_o}(1-\frac{\rho'}{\rho_o})(-\rho_o g+\frac{\partial P'}{\partial z})-g \\ &= -\frac{1}{\rho_o}\frac{\partial P'}{\partial z}-\frac{\rho'}{\rho_o}g\end{aligned} \tag{2.7}$$

Further simplifications can be made by employing the equation of state for moist air

$$P=\rho R_d T(1+0.61q_v) \tag{2.8}$$

where R_d is the gas constant for dry air and q_v is the water vapour mixing ratio.

Taking the logarithm of (2.8), and differentiating yields

$$\frac{\rho'}{\rho_o}=\frac{P'}{P_o}-\frac{T'}{T_o}-0.61q_v' \tag{2.9}$$

Substituting (2.7) and (2.9) into (2.2) to (2.4) and using the basic assumptions listed in Section 2.1, we obtain

$$\frac{\partial u'}{\partial t}+u'\frac{\partial u'}{\partial x}+w'\frac{\partial u'}{\partial z}=-\frac{1}{\rho_o}\frac{\partial P'}{\partial x}+fv'+F_x \tag{2.10}$$

$$\frac{\partial v'}{\partial t}+u'\frac{\partial v'}{\partial x}+w'\frac{\partial v'}{\partial z}+u'\frac{\partial v_o}{\partial x}+w'\frac{\partial v_o}{\partial z}=-fu'+F_y \tag{2.11}$$

$$\frac{\partial w'}{\partial t}+u'\frac{\partial w'}{\partial x}+w'\frac{\partial w'}{\partial z}=-\frac{1}{\rho_o}\frac{\partial P'}{\partial z}+\beta+F_z \tag{2.12}$$

where

$$\beta=g(\frac{T'}{T_o}+0.61q_v'-q_l-\frac{P'}{P_o}) \tag{2.13}$$

is the total buoyancy.

By using (2.1), (2.10) to (2.12) can be written in flux form. So finally,

$$\frac{\partial u'}{\partial t}+\frac{\partial}{\partial x}(u'u')+\frac{1}{\rho_o}\frac{\partial}{\partial z}(\rho_o u'w')=-\frac{1}{\rho_o}\frac{\partial P'}{\partial x}+fv'+F_x \tag{2.14}$$

$$\frac{\partial v'}{\partial t}+\frac{\partial}{\partial x}(u'v')+\frac{1}{\rho_o}\frac{\partial}{\partial z}(\rho_o v'w')+u'\frac{\partial v_o}{\partial x}+w'\frac{\partial v_o}{\partial z}=-fu'+F_y \tag{2.15}$$

$$\frac{\partial w'}{\partial t}+\frac{\partial}{\partial x}(u'w')+\frac{1}{\rho_o}\frac{\partial}{\partial z}(\rho_o w'w')=-\frac{1}{\rho_o}\frac{\partial P'}{\partial z}+\beta+F_z \tag{2.16}$$

(3) Water substances equation

By using the continuity equation, the conservation equation for total water substance $q = q_v + q_l$ is

$$\frac{\partial q}{\partial t}+\frac{\partial}{\partial x}(u'q)+\frac{1}{\rho_o}\frac{\partial}{\partial z}(\rho_o w'q)=F_q \tag{2.17}$$

where F_q is the turbulence term.

(4) Thermodynamic equation

Similarly, the conservation of total entropy ϕ is

$$\frac{\partial \phi}{\partial t}+\frac{\partial}{\partial x}(u'\phi)+\frac{1}{\rho_o}\frac{\partial}{\partial z}(\rho_o w'\phi)=F_\phi \tag{2.18}$$

where

$$\begin{aligned}\phi=&C_{pd}\ln\left(\frac{\theta}{\theta_b}\right)+\frac{Lq_v}{T}\\&+C_l q_v\ln\left(\frac{T}{T_b}\right)+C_l q_l\ln\left(\frac{T}{T_b}\right)\end{aligned} \tag{2.19}$$

θ_b and T_b are respectively the reference potential temperature and temperature, both set equal to 200 K. C_{pd} and C_l are the specific heats at constant pressure for dry air and liquid water respectively. As described by Steiner (1982) the deviation of ϕ from its basic state can be approximated by

$$\phi'=\left(C_{pd}-\frac{L}{T_o}q_{vo}\right)\frac{T'}{T_o}-R_d\frac{P'}{P_o}+\frac{Lq_v'}{T_o} \tag{2.20}$$

This equation will be used for the saturation analysis.

(5) Saturation analysis

In this model the only moisture quantity used as an independent variable is the total water mixing ratio. To calculate the buoyancy term in (2.12), we must know q_v' and q_l. The procedure to determine q_l is as follows.

First, (2.17) and (2.18) are integrated in time to determine new values of q and ϕ. Then, on the assumption that the air is not saturated, we use (2.20) to calculate T' assuming $P' = 0$. The new value of $T = T_0 + T'$ can then be used to calculate the new saturation mixing ratio q_{vs} through an approximation such as Teten's formula. If this value of q_{vs} does exceed q, as we assumed, then the air is indeed unsaturated and $q_v = q$, $q_l = 0$. However, if q_{vs} is less than q, then we set $q_v = q_{vs}$ and $q_l = q - q_v$, and recalculate T' using (2.20). This, of course, assumes that q_{vs} is relatively insensitive to the change in T'.

(6) Parameterization of turbulence

The turbulence terms in (2.14) to (2.18) can be derived as subgrid-scale processes by averaging the original inviscid governing equations. Let Q be the sum of a grid volume average (denoted by $\bar{}$) plus a deviation (denoted by *)

$$Q(x,z) = \bar{Q} + Q^* \tag{2.21}$$

where the averaging operator is

$$\bar{Q} = \frac{1}{\Delta x \cdot \Delta z} \int_{x-\Delta x/2}^{x+\Delta x/2} \int_{z-\Delta z/2}^{z+\Delta z/2} Q \, dz \, dx \tag{2.22}$$

By applying (2.21) and (2.22) to a typical nonlinear term such as $\partial(u\phi)/\partial x$ and by assuming that $\overline{Q^*} = 0$, we get

$$\begin{aligned} \overline{\frac{\partial}{\partial x}(u\,\phi)} &= \overline{\frac{\partial}{\partial x}\bar{u}\,\bar{\phi} + \frac{\partial}{\partial x}\bar{u}\,\phi^* + \frac{\partial}{\partial x}u^*\,\bar{\phi} + \frac{\partial}{\partial x}u^*\,\phi^*} \\ &= \frac{\partial}{\partial x}\bar{u}\,\bar{\phi} + \frac{\partial}{\partial x}\overline{u^*\,\phi^*} \end{aligned} \tag{2.23}$$

where $\overline{u^*\phi^*}$ represents the redistribution of ϕ by unresolvable (subgrid) horizontal motion u^* and is termed the subgrid scale flux of ϕ. This quantity is by definition unknown and we must use a closure scheme to estimate its value. The most common scheme is to assume that the subgrid fluxes are proportional to the gradients of the resolvable scales,

$$\overline{u^{*}\phi^{*}} = -\nu_{s}\frac{\partial\bar{\phi}}{\partial x} \tag{2.24}$$

where ν_{s} is the exchange coefficient for a scalar variable.

The governing equations then become

$$\begin{aligned}
\frac{d\bar{u}}{dt} &= -\frac{1}{\bar{\rho}}\frac{\partial\bar{P}}{\partial x}+f\bar{v}-\frac{1}{\bar{\rho}}\left(\frac{\partial}{\partial x}\overline{\rho u^{*}u^{*}}+\frac{\partial}{\partial y}\overline{\rho u^{*}v^{*}}+\frac{\partial}{\partial z}\overline{\rho u^{*}w^{*}}\right)\\
\frac{d\bar{v}}{dt} &= -\frac{1}{\bar{\rho}}\frac{\partial\bar{P}}{\partial y}-f\bar{u}-\frac{1}{\bar{\rho}}\left(\frac{\partial}{\partial x}\overline{\rho v^{*}u^{*}}+\frac{\partial}{\partial y}\overline{\rho v^{*}v^{*}}+\frac{\partial}{\partial z}\overline{\rho v^{*}w^{*}}\right)\\
\frac{d\bar{w}}{dt} &= -\frac{1}{\bar{\rho}}\frac{\partial\bar{P}}{\partial z}-g-g\bar{q}_{l}-\frac{1}{\bar{\rho}}\left(\frac{\partial}{\partial x}\overline{\rho w^{*}u^{*}}+\frac{\partial}{\partial y}\overline{\rho w^{*}v^{*}}+\frac{\partial}{\partial z}\overline{\rho w^{*}w^{*}}\right)\\
\frac{d\bar{q}}{dt} &= -\frac{1}{\bar{\rho}}\left(\frac{\partial}{\partial x}\overline{\rho q^{*}u^{*}}+\frac{\partial}{\partial y}\overline{\rho q^{*}v^{*}}+\frac{\partial}{\partial z}\overline{\rho q^{*}w^{*}}\right)\\
\frac{d\bar{\phi}}{dt} &= -\frac{1}{\bar{\rho}}\left(\frac{\partial}{\partial x}\overline{\rho\phi^{*}u^{*}}+\frac{\partial}{\partial y}\overline{\rho\phi^{*}v^{*}}+\frac{\partial}{\partial z}\overline{\rho\phi^{*}w^{*}}\right)
\end{aligned} \tag{2.25}$$

where

$$\begin{aligned}
\overline{\rho u^{*}u^{*}} &= -\bar{\rho}\nu_{m}\left(\frac{\partial\bar{u}}{\partial x}+\frac{\partial\bar{u}}{\partial x}\right), & \overline{\rho u^{*}w^{*}} &= -\bar{\rho}\nu_{m}\left(\frac{\partial\bar{u}}{\partial z}+\frac{\partial\bar{w}}{\partial x}\right),\\
\overline{\rho v^{*}u^{*}} &= -\bar{\rho}\nu_{m}\left(\frac{\partial\bar{v}}{\partial x}\right), & \overline{\rho v^{*}w^{*}} &= -\bar{\rho}\nu_{m}\left(\frac{\partial\bar{v}}{\partial z}\right),\\
\overline{\rho w^{*}u^{*}} &= \overline{\rho u^{*}w^{*}}, & \overline{\rho w^{*}w^{*}} &= -\bar{\rho}\nu_{m}\left(\frac{\partial\bar{w}}{\partial z}+\frac{\partial\bar{w}}{\partial z}\right),\\
\overline{\rho q^{*}u^{*}} &= -\bar{\rho}\nu_{s}\frac{\partial\bar{q}}{\partial x}, & \overline{\rho q^{*}w^{*}} &= -\bar{\rho}\nu_{s}\frac{\partial\bar{q}}{\partial z},\\
\overline{\rho\phi^{*}u^{*}} &= -\bar{\rho}\nu_{s}\frac{\partial\bar{\phi}}{\partial x}, & \overline{\rho\phi^{*}w^{*}} &= -\bar{\rho}\nu_{s}\frac{\partial\bar{\phi}}{\partial z}
\end{aligned} \tag{2.26}$$

ν_{m} is the exchange coefficient for momentum variables. In our experiments we take $\nu_{m} = \nu_{s} = 1\ \mathrm{m}^{2}\,\mathrm{s}^{-1}$.

Finally , by substituting (2.26) into (2.25) and by dropping the overbar sign the turbulence terms take the final form

$$
\begin{aligned}
F_x &= \frac{\partial}{\partial x}(2\nu_m\frac{\partial u}{\partial x})+\frac{1}{\rho_o}\frac{\partial}{\partial z}(\rho_o\nu_m(\frac{\partial u}{\partial z}+\frac{\partial w}{\partial x}))\\
F_y &= \frac{\partial}{\partial x}(\ \nu_m\frac{\partial v}{\partial x})+\frac{1}{\rho_o}\frac{\partial}{\partial z}(\rho_o\nu_m\frac{\partial v}{\partial z})\\
F_z &= \frac{\partial}{\partial x}(\nu_m(\frac{\partial u}{\partial z}+\frac{\partial w}{\partial x}))+\frac{1}{\rho_o}\frac{\partial}{\partial z}(2\rho_o\nu_m\frac{\partial w}{\partial z})\\
F_q &= \frac{\partial}{\partial x}(\ \nu_s\frac{\partial q}{\partial x})+\frac{1}{\rho_o}\frac{\partial}{\partial z}(\rho_o\nu_s\frac{\partial q}{\partial z})\\
F_\phi &= \frac{\partial}{\partial x}(\ \nu_s\frac{\partial \phi}{\partial x})+\frac{1}{\rho_o}\frac{\partial}{\partial z}(\rho_o\nu_s\frac{\partial \phi}{\partial z})
\end{aligned}
\tag{2.27}
$$

(7) The pressure equation

A diagnostic equation for p' can be obtained by combining $\partial/\partial x\ [\rho_0(2.14)]$ and $\partial/\partial z\ [\rho_0(2.16)]$,

$$
\begin{aligned}
(\frac{\partial^2}{\partial x^2}+\frac{\partial^2}{\partial z^2})\ P' = &\frac{\partial}{\partial x}\rho_o A_x+\frac{\partial}{\partial z}\rho_o A_z+\frac{\partial}{\partial x}\rho_o F_x+\frac{\partial}{\partial z}\rho_o F_z\\
&+\frac{\partial}{\partial z}\rho_o\beta+\frac{\partial}{\partial x}\rho_o f v'-\frac{\partial}{\partial t}D
\end{aligned}
\tag{2.28}
$$

where

$$A_x=-(\frac{\partial}{\partial x}(u'u')+\frac{1}{\rho_o}\frac{\partial}{\partial z}(\rho_o u'w')) \tag{2.29}$$

$$A_z=-(\frac{\partial}{\partial x}(w'u')+\frac{1}{\rho_o}\frac{\partial}{\partial z}(\rho_o w'w')) \tag{2.30}$$

$$D=\rho_o\frac{\partial u'}{\partial x}+\frac{\partial}{\partial z}(\rho_o w') \tag{2.31}$$

Strictly speaking, p' must be known before the buoyancy term in (2.28), $\partial/\partial z\,(\rho_0\ \beta)$, can be evaluated. However, Ogura and Wilhelmson (1972) showed that the contribution of p' in determining the buoyancy is small and can be replaced by its value at a previous time step. Therefore, we use the p' term calculated at a previous time step to determine the buoyancy term on the right of (2.28).

The last term in (2.28), $-\partial/\partial t$ D, the local rate of change of the divergence of the mass flux, should be identically zero but is unlikely to be so in the numerical integration due to truncation errors. Following the method of Harlow and Welch (1965), we retain this term as a negative feedback. Specifically, we write it as $(D^{n+1}-D^{n-1})/(2\Delta t)$ and assume $D^{n+1}=0$ to ensure that the divergence of the mass flux remains small and does not increase with time.

2.3 Boundary conditions

(1) Vertical boundary conditions

The top and bottom boundaries are assumed rigid, perfectly insulated and free-slip. thus

$$w'=\frac{\partial u'}{\partial z}=\frac{\partial v'}{\partial z}=\frac{\partial \phi}{\partial z}=\frac{\partial q}{\partial z}=0, \qquad at \quad z=0, \quad or \quad z=H \tag{2.32}$$

Substituting (2.32) into (2.12) yields a boundary condition for the pressure

$$-\frac{1}{\rho_o}\frac{\partial P'}{\partial z}+\beta=0, \qquad at \quad z=0, \quad or \quad z=H \tag{2.33}$$

(2) Lateral boundary conditions

The lateral boundaries are also assumed rigid, perfectly insulated and free-slip, with

$$u'=\frac{\partial v'}{\partial x}=\frac{\partial \phi}{\partial x}=\frac{\partial q}{\partial x}=\frac{\partial w'}{\partial x}=0, \qquad at \quad x=-L, \quad or \quad x=L \tag{2.34}$$

2.4 Grid system and finite difference methods

(1) Grid system

A staggered grid is used. The wind velocities u and w are placed at the sides of the grid boxes and all the other variables at the centre. The physical domain is 900 km X 10 km. The horizontal grid length is 10 km. The vertical grid length, which is different for different cases, varies from 62.5 m to 250 m (see Chapter 3 for more details).

(2) Finite difference methods

Using the notation that

$$\begin{aligned} \delta_x F &= (F_{i+1/2} - F_{i-1/2})/\Delta x \\ \delta_z F &= (F_{j+1/2} - F_{j-1/2})/\Delta z \\ \overline{F}^x &= (F_{i+1/2} + F_{i-1/2})/2 \\ \overline{F}^z &= (F_{j+1/2} + F_{j-1/2})/2 \\ \delta_{2t} F &= (F^{n+1} - F^{n-1})/(2\Delta t) \end{aligned} \tag{2.35}$$

(2.14) to (2.18) can be written as

$$\delta_{2t}\, u' = A_x^n + F_x^{n-1} - \frac{1}{\rho_o}\delta_x (P')^n + f(\overline{v'}^x)^n \tag{2.36}$$

$$\delta_{2t}\, v' = A_y^n + F_y^{n-1} - f(\overline{u'}^x)^n - (u')^n \delta_x \overline{v_o}^x - (w')^n \delta_z \overline{v_o}^x \tag{2.37}$$

$$\delta_{2t}\, w' = A_z^n + F_z^{n-1} - \frac{1}{\rho_o}\delta_z (P')^n + (\overline{\beta}^z)^n \tag{2.38}$$

$$\delta_{2t}\, q = A_q^n + F_q^{n-1} \tag{2.39}$$

$$\delta_{2t}\, \phi = A_\phi^n + F_\phi^{n-1} \tag{2.40}$$

where

$$
\begin{aligned}
A_x&=-\delta_x(\overline{u'}^x\,\overline{u'}^x)-\frac{1}{\rho_o}\delta_z(\rho_o\overline{u'}^z\,\overline{w'}^x)\\
A_y&=-\delta_x(u'\,\overline{v'}^x)-\frac{1}{\rho_o}\delta_z(\rho_o\overline{v'}^z\,w')\\
A_z&=-\delta_x(\overline{u'}^z\,\overline{w'}^x)-\frac{1}{\rho_o}\delta_z(\rho_o\overline{w'}^z\,\overline{w'}^z)\\
A_q&=-\delta_x(u'\,\bar{q}^x)-\frac{1}{\rho_o}\delta_z(\rho_o w'\,\bar{q}^z)\\
A_\phi&=-\delta_x(u'\,\bar{\phi}^x)-\frac{1}{\rho_o}\delta_z(\rho_o w'\,\bar{\phi}^z)\\
F_x&=\delta_x(2\nu\delta_x u)+\frac{1}{\rho_o}\delta_z(\rho_o\nu(\delta_z u+\delta_x w))\\
F_y&=\delta_x(\ \nu\delta_x v)+\frac{1}{\rho_o}\delta_z(\rho_o\nu\delta_z v)\\
F_z&=\delta_x(\nu(\delta_z u+\delta_x w))+\frac{1}{\rho_o}\delta_z(2\rho_o\nu\delta_z w)\\
F_q&=\delta_x(\nu\delta_x q)+\frac{1}{\rho_o}\delta_z(\rho_o\nu\delta_z q)\\
F_\phi&=\delta_x(\nu\delta_x\phi)+\frac{1}{\rho_o}\delta_z(\rho_o\nu\delta_z\phi)
\end{aligned}
\tag{2.41}
$$

The diffusion terms are calculated at the (n-1)th time step to avoid numerical instability and $\Delta t = 15$ s is used.

The pressure equation (2.28) becomes

$$
\begin{aligned}
(\delta_z\delta_z+\delta_x\delta_x)(P')^n &= \rho_o\delta_x[A_x^n+F_X^{n-1}+f(\overline{v'}^x)^n]\\
&\quad+\frac{\partial}{\partial z}[\rho_o(A_z^n+F_z^n+(\overline{\beta}^z)^n)]+\frac{D^{n-1}}{2\Delta t}
\end{aligned}
\tag{2.42}
$$

where

$$D=\rho_o\delta_x u'+\delta_z(\rho_o w') \tag{2.43}$$

Also, the boundary conditions (2.32), (2.33) and (2.34) can be rewritten as

$$
\begin{aligned}
w'=\delta_z u'=\delta_z v'=\delta_z\phi=\delta_z q=0,&\qquad at\ \ z=0\ \ or\ \ z=H\\
-\frac{1}{\rho_o}\delta_z P'+\overline{\beta}^z=0,&\qquad at\ \ z=0\ \ or\ \ z=H\\
u'=\delta_x v'=\delta_x\phi=\delta_x q=\delta_x w'=0,&\qquad at\ \ x=-L\ \ or\ \ x=L
\end{aligned}
\tag{2.44}
$$

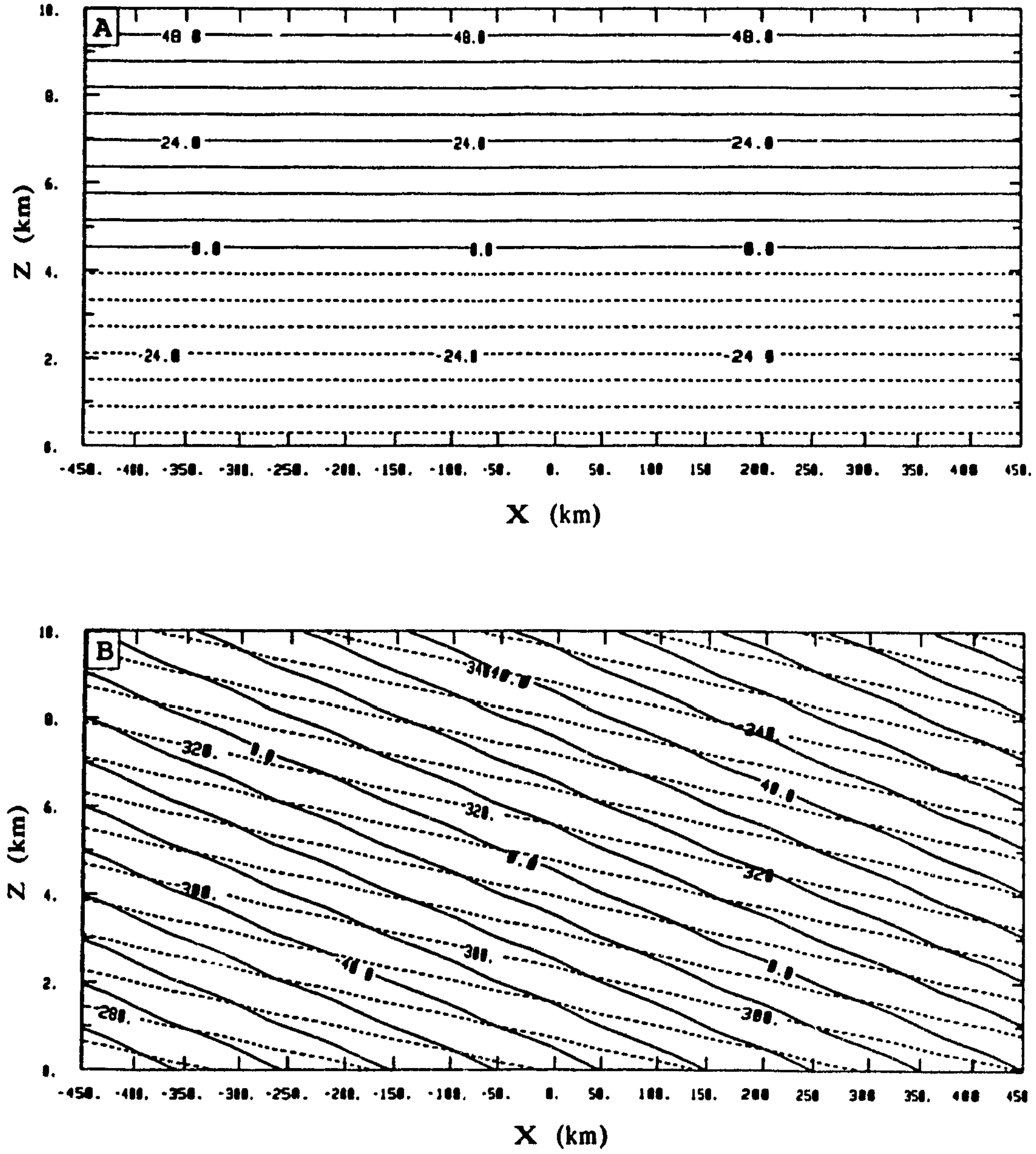

Fig. 2.1. Basic state with PV = 0.3 pvu (10^{-6} K m^2 kg^{-1} s^{-1}) and $\partial v/\partial z = 0.01$ s^{-1}. (A) v component of velocity (unit: m s^{-1}); (B) Absolute momentum M (solid lines, in m s^{-1}) and potential temperature θ (dashed lines, in K).

CHAPTER 3

EXPERIMENTS, RESULTS AND DISCUSSION

3.1 Initialization

The purpose of the initialization for the study of pure conditional symmetric instability is to obtain an initial state which is stable for dry symmetric instability (while also convectively and inertially stable) but potentially unstable for moist symmetric instability. Also, an impulse is needed to release the instability in a reasonable time span.

The basic state values for v, M, θ, P, and T were specified in section 2.1 (2). The relative humidity profile is assumed uniform in x and is specified by "trial-and-error" to satisfy the conditions that $\partial\theta_e/\partial z \geq 0$ in the whole domain and $PV_{\theta e} < 0$ in some part of it. The vertical distribution of relative humidity is tabulated in Table 3.1 and depicted graphically in Fig. 3.1(A). Its value increases from 0 % at the top of the domain to 100 % at and below about 0.5 km. The moist potential vorticity, $PV_{\theta e}$, in Fig. 3.1(C) varies from 0.25 pvu at the upper-left corner to -1.13 pvu at the lower-right corner. The values of equivalent potential vorticity and relative humidity near the centre of the impulse are -0.48 pvu and 98 %, respectively. Fig. 3.1(B) shows that $\partial\theta_e/\partial z \geq 0$ everywhere in the domain. The basic state is therefore convectively stable although a small region from 3 km to 7 km near the right boundary exhibits near neutral stratification to upright convection.

The velocity impulse is depicted in Fig. 3.2. For its specification, we first select a streamfunction of the form

$$\psi=-0.5\psi_o(kx+z)\{1+\cos[2\pi(z-z_o)/H]\}\exp[-A(kx+z)^2] \tag{3.1}$$

where ψ_0, A, k are constants. z_0 and H represent the height of the centre of the impulse and its depth respectively. ψ_0 determines the amplitude of the impulse. The value for k is chosen so that the axis of the impulse lies within a wedge bounded by an M and a θ_e surface. A determines the horizontal extent of the impulse.

To satisfy continuity, we calculate u' and w' from $\rho_0 u'=\partial\psi/\partial z$ and $\rho_0 w'=-\partial\psi/\partial x$. With H = 3000 m, A = 4.05×10^{-7} m^{-2}, k = 1.5873×10^{-2} and ψ_0 = 1750 kg m^{-1} s^{-1}, the maximum and minimum values for w' and u' are (0.049 m s^{-1}, -0.022 m s^{-1}) and (2.55 m s^{-1}, -3.10 m s^{-1}), respectively. u' is shown in Fig.3.2(C).

3.2 Vertical resolution

In a simulation of slantwise convection using a hydrostatic model, Persson and Warner (1991) found that spurious gravity waves can be generated if the vertical and horizontal resolution is not consistent. For consistency, they proposed the following formula relating Δx and Δp

$$AS = \frac{\Delta p\ /\Delta x}{s} = 1 \tag{3.2}$$

where Δp, Δx are vertical and horizontal grid lengths and s is the slope in pressure coordinates of zones of enhanced or decreased horizontal temperature gradients ('fronts') that may develop during the simulation.

In height coordinates, (3.2) becomes

$$AS = \frac{\Delta z\ /\ \Delta x}{s_z} = 1\ , \tag{3.3}$$

where Δz is the vertical grid length and s_z is the slope of the 'front' in height coordinates. For $\Delta x = 10$ km and $s_z = 1/80$, Δz calculated from (3.3) is 125 m. This criterion translates into 80 vertical levels for a domain height of 10 km. We have carried out three simulations using respectively 40, 80, and 160 vertical levels. Our presentation would focus on the 160 layer simulation L160 (Δz=62.5 m) which exhibits the smoothest solution among the three runs. Plots for the other runs (simulation L80, Δz=125 m and simulation L40, Δz=250 m) would also be presented for comparison.

3.3 Results and discussion

Simulation L160 was run for 37 hours. During this period the CSI circulation experienced its onset, growth, mature and decay stages.

(1) Evolution of w_{max}

w_{max} decreases from an initial value of 4.9 cm s^{-1} to 2.1 cm s^{-1} during the first 6 hours (Fig. 3.3). The amount of condensation is relatively small and the initial impulse is dissipating gradually. From 6 h to 25 h the circulation develops rapidly and the maximum vertical velocity reaches 15 cm s^{-1} at 28 h. Three hours later, the CSI circulation begins its decay and w_{max} decreases to 10.5 cm s^{-1} by 37 h.

For discussion purposes, we shall refer to the first 6 hours as the onset stage, the period from 6 h to 25 h as the growth stage. The mature stage spans from 25 h to 31 h and is followed by the decaying stage thereafter.

(2) Development of the cloudband

The cloud water mixing ratio is displayed every 2 hours in Fig. 3.4. Within the first 4 hours, a relatively weak slanted cloudband has formed. The band develops rapidly especially between 10 h and 26 h. The location of the band coincides with the location of the narrow slanted updraft discussed in section 3.3.(3). The maximum cloud water mixing ratio near the leading edge of cloud reaches 9 g kg^{-1} at 28 h. This large value can be attributed to the absence of precipitation mechanism in the model which would result in the fallout of precipitation. After 28 h, downdrafts begin to develop at the lower portion of the band and the decay of the cloud gradually sets in. However, the upper portion of the band continues to persist till 37 h when the simulation terminates.

(3) Evolution of the CSI circulation

The evolution of the transverse CSI circulation is shown by the vertical cross sections of streamfunction ψ, and vertical velocity w in Figs. 3.5 - 3.8.

At 5 h, the initial impulse has weakened considerably but the slantwise ascending flow remains with a maximum vertical motion of 2.55 cm s^{-1}.The axis of the updraft is leaning toward the initial absolute momentum surfaces (compare Fig. 3.5(A) with Fig. 3.2(A) and 3.1(B)). During the growing stage at 21 h, the streamfunction shows a very narrow, well-defined sloping updraft with a relatively strong maximum vertical velocity of 13.4 cm s^{-1} (Fig. 3.6). It is of interest to note that a strong and extremely narrow downdraft is located immediately above the updraft. The axis of the updraft still lies between the M and θ_e surfaces but it is clear that its inclination is more horizontal than that in its initial configuration. By 28 h (Fig. 3.7), the circulation has reached its mature stage. The updraft is extending to an altitude of 8 km. Two downdrafts are evident; a stronger one above the updraft and a weaker one below. Vertical convective cells can be identified in the cloudband at the (x,z) locations around (70 km, 3 km) and (-125 km, 6 km). The strength and the extent of the circulation lessen considerably during the decaying stage around 34 h (Fig. 3.8) and downdrafts develop at the lower portion of the cloudband.

(4) Evolution of the instability

The evolution of convective, inertial and CSI will be assessed from the distributions of the θ_e, M, and $PV_{\theta e}$ surfaces.

Fig. 3.9 show the cross sections of M and θ_e. From an initially stable stratification for upright convection, a convectively unstable layer near the top of the cloudband has developed by 5 h (Fig. 3.9(A)). The model is trying to release this instability as can be seen from the small vertical updraft located near $x = 270$ km and $z = 1.8$ km in Fig. 3.5(B). At 21 h, the M surfaces also undergo significant deformation in the region of the cloudband (Fig. 3.9(B)). There is a general tendency for the M and θ_e surfaces to run parallel to one another within the slanted updraft even at 28 h and 34 h (Figs. 3.9(C) and (D)).

The mechanism for the formation of the convectively unstable layer is illustrated schematically in Fig. 3.10. The slantwise circulation occurs at an angle to the θ_e surfaces. The advection of the equivalent potential temperature surfaces by the strong slanted up and downdrafts gives rise to a region of convective instability near the top of the band and a region of convective stability near its bottom. This type of destabilization is also noted by Bennetts and Hoskins (1979) and Saitoh and Tanaka (1987) in their numerical simulations. In fact, the latter authors suggested that convective clouds which develop in the mid-tropospheric convectively unstable layer above the stratiform cloudband can enhance the seeder-feeder precipitation mechanism in some rainbands.

The effects of the CSI circulation on convective and inertial instabilities can be further illustrated from the $\partial\theta_e/\partial z$ and $\partial M/\partial x$ plots in Figs. 3.11 and 3.12. While the convectively unstable region mainly develops within the upper half of the band, areas of inertial instability resulting from the advection of M surfaces can be located both near the cloudtop and near the bottom of the cloudband. A magnified view at 31 h is shown in Fig. 3.13. Regions of convective (Fig.3.13(A)) and inertial (Fig. 3.13(B)) instabilities are shaded. Vertical convective cells (at x= -150 km, z = 6.5 km and around $0 < x < 100$ km and 2.5 km $< z <$ 4.5 km) embedded in the generally slanted cloudband are evident in the distribution of cloud water content in Fig. 3.13(C).

In saturated regions, CSI is characterized by negative moist potential vorticity (MPV). An equation for the domain averaged MPV can be derived using the momentum, thermodynamic and continuity equations with appropriate boundary conditions. It has the form

$$\begin{aligned}\frac{\partial}{\partial t}<\rho_0 PV_{\theta e}> = \frac{1}{2LH}\int_{-L}^{L}[\theta_e\frac{\partial F_y}{\partial x}-M\frac{\partial F_{\theta_e}}{\partial x} \\ -\frac{2Mv_s}{\theta_e}(\frac{\partial\theta_e}{\partial x}\frac{\partial^2\theta_e}{\partial x^2}+\frac{\partial\theta_e}{\partial z}\frac{\partial^2\theta_e}{\partial x\partial z})]_0^H\,dx \\ -\frac{1}{2LH}\int_0^H[\rho_0 u\ PV_{\theta_e}+\theta_e\frac{\partial F_y}{\partial z}-M\frac{\partial F_{\theta_e}}{\partial z} \\ -\frac{2Mv_s}{\theta_e}(\frac{\partial\theta_e}{\partial z}\frac{\partial^2\theta_e}{\partial z^2}+\frac{\partial\theta_e}{\partial x}\frac{\partial^2\theta_e}{\partial x\partial z})]_{-L}^{L}\,dz\end{aligned} \tag{3.4}$$

where

$$F_{\theta_e}\equiv\frac{\partial}{\partial x}(v_s\frac{\partial\theta_e}{\partial x})+\frac{1}{\rho_0}\frac{\partial}{\partial z}(\rho_0 v_s\frac{\partial\theta_e}{\partial z})$$

$$<\ \ >\equiv\frac{1}{2LH}\int_0^H\int_{-L}^{L}(\ \ )dxdz$$

Eq. (3.4) indicates that the domain averaged $PV_{\theta e}$ can be changed only by boundary fluxes of $PV_{\theta e}$ and turbulence effects. Fig. 3.14 shows that during the onset and growth stages the domain averaged $PV_{\theta e}$ decreases slightly, but increases during the mature and decay stages. Although this trend is clear from the plot, the magnitude of the change is relatively small and amounts to only about 1 %.

The detailed evolution of $PV_{\theta e}$ is depicted in Fig. 3.15. At 5 h, the -0.5 pvu isoline exhibits a "W" pattern as the updraft transports low value of $PV_{\theta e}$ upward and the downdrafts transport high value of $PV_{\theta e}$ downward. This transport intensifies at 21 h and regions of positive and negative $PV_{\theta e}$ can be found in the cloudband. A similar behavior can be found at 28 h and 34 h when the cloud penetrates into areas with positive MPV. It is probable that the positive and negative MPV anomalies are caused by turbulent diffusion. Indeed, Thorpe and Rotunno (1989) has shown that in dry case, turbulence achieves a downgradient mixing of heat and momentum but can lead to an upgradient mixing of PV.

(5) Energetics

The energetics of the system will be examined from the kinetic energy budget. We first decompose the total perturbation kinetic energy (TKE) into the along-band (y direction) perturbation kinetic energy (KEY) and the transverse perturbation kinetic energy (KEXZ) :

$$\underbrace{\frac{1}{2}<\rho_0 u'^2+\rho_0 v'^2+\rho_0 w'^2>}_{TKE} = \underbrace{\frac{1}{2}<\rho_0 u'^2+\rho_0 w'^2>}_{KEXZ} + \underbrace{\frac{1}{2}<\rho_0 v'^2>}_{KEY} \tag{3.5}$$

where < > represents the domain average operator:

$$< > = \frac{1}{2LH}\int_0^H\int_{-L}^{L}(\ )dx\, dz$$

Fig.3.16 shows the time evolutions of TKE, KEXZ and KEY. It is clear that KEXZ, related directly to the strength of the transverse CSI circulation, undergoes a four stage development similar to that of the maximum vertical velocity field: initial onset stage (0 h - 7 h), growth stage (7 h - 27 h), mature stage (27 h - 35 h) and decay stage (35 h - 37 h). The behavior of TKE is quite similar to that of KEY.

The KEY term, representing the energy conversion between the mean flow and the transverse CSI circulation, increases slowly during the first 15 h and then more rapidly up to 30 h. A smooth decay follows after 30 h. Despite the fact that KEY peaks about 6 hours earlier than KEXZ, they are of the same order of magnitude.

The details of energy conversion is given by the equation governing the time rate of change of domain averaged TKE. The equation can be obtained readily by multiplying (2.10), (2.11), and (2.12) respectively by $\rho_0\, u'$, $\rho_0\, v'$ and $\rho_0\, w'$; adding the results and then taking the domain average. Its form is

$$\underset{DKDT}{\frac{\partial}{\partial t}<\frac{\rho_0}{2}(u'^2+v'^2+w'^2)>} = \underset{BUO}{<\rho_0 B w'>} + \underset{DIS}{<\rho_0(u'F_x+v'F_y+w'F_z)>} - \underset{SH}{<\rho_0 v'w'\frac{\partial v_0}{\partial z}>} \tag{3.6}$$

BUO is the buoyancy generation term, representing the conversion from potential to kinetic energy by warm air rising and cold air sinking. DIS is the dissipation term, representing the work done by the turbulent stresses. SH is the shear generation term, describing the conversion from basic state kinetic energy to perturbation kinetic energy.

Fig. 3.17(B) shows that before a substantial amount of condensation occurs, BUO is negative from 0 to 3 h. A positive BUO due to latent heat release after 3 h is responsible for reversing the decay of the DKDT term. While the shear term represents a sink for perturbation kinetic energy up to 6 h, it is by far the most important source term thereafter (see Fig. 3.17 A). The dissipation term acts as a sink throughout the simulation and is especially large from 27 to 31 h when the transverse CSI circulation is well developed.

In the first 15 h, the buoyancy term is relatively small but positive and is most important in releasing the instability which develops the CSI circulation. After 15 h, most of the perturbation kinetic energy is obtained from the mean flow. The buoyancy term becomes negative after 24 h. Together with the increasing dissipation, they are responsible for the decay of the system and a weakening of the shear generation term after 27 h.

(6) Consistency of vertical and horizontal grid resolutions

To determine the effect of varying the vertical grid size for a given horizontal resolutions of 10 km, we display the vertical velocity at 28 h for simulations L160, L80, and L40 in Fig. 3.18. The vertical grid length for the three runs are 62.5 m, 125 m and 250 m, respectively. The AS ratios estimated using the approximated equation (3.3) are 0.5, 1 and 2 for the three experiments. The vertical velocity field is shown because it is the most sensitive parameter to changes in the AS ratio.

Fig. 3.18(A) shows a well-defined sloping circulation. The vertical convective cell around $x = -125$ km and $z = 6$ km sets off gravitational oscillations below 6 km around $x = -150$ km. In comparison, the w field is relatively noisy in L80 (Fig. 3.18(B)), while in L40, the CSI circulation is completely masked (Fig. 3.18(C)). In terms of the extreme values, the maximum and minimum w velocities in m s^{-1} are (+0.14, -0.20) in L80 and (+0.14, -0.14) in L160. However, in L80, short-wavelength gravity waves can be found in and near the slanted circulation. Persson and Warner (1991) pointed out that 'the selection of a vertical grid spacing for a numerical simulation should not be done without considering the horizontal grid spacing, the likely occurrence of narrow sloping frontlike structures, and the AS ratio. ' Our results lend support to their conclusions.

Table 3.1. Initial distribution of relative humidity RH(z).

Height (m)	RH (%)
10000	0.0
9500	14.3
9000	27.1
8500	38.6
8000	48.8
7500	57.8
7000	65.7
6500	72.5
6000	78.4
5500	83.4
5000	87.5
4500	90.9
4000	93.6
3500	95.7
3000	97.3
2500	98.4
2000	99.2
1500	99.7
1000	99.9
500	100.0
0	100.0

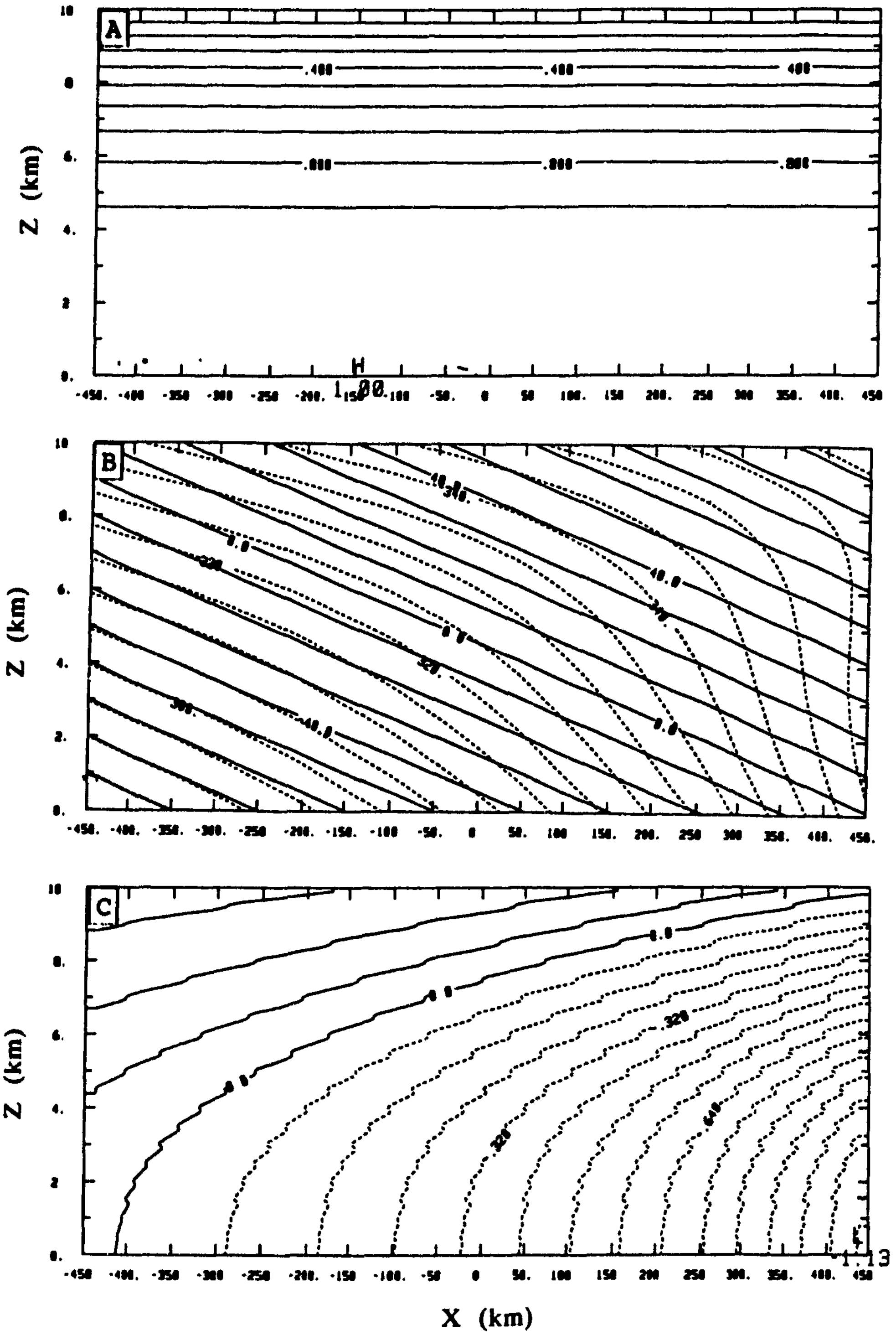

Fig. 3.1. The initial fields. (A) Relative humidity. Contour interval is 10 %. (B) Equivalent potential temperature (dashed, contour interval is 5 K) and absolute momentum (solid, contour interval is 10 m s^{-1}). (C) Equivalent potential vorticity. Negative contours are dashed. Contour interval is 0.08 pvu.

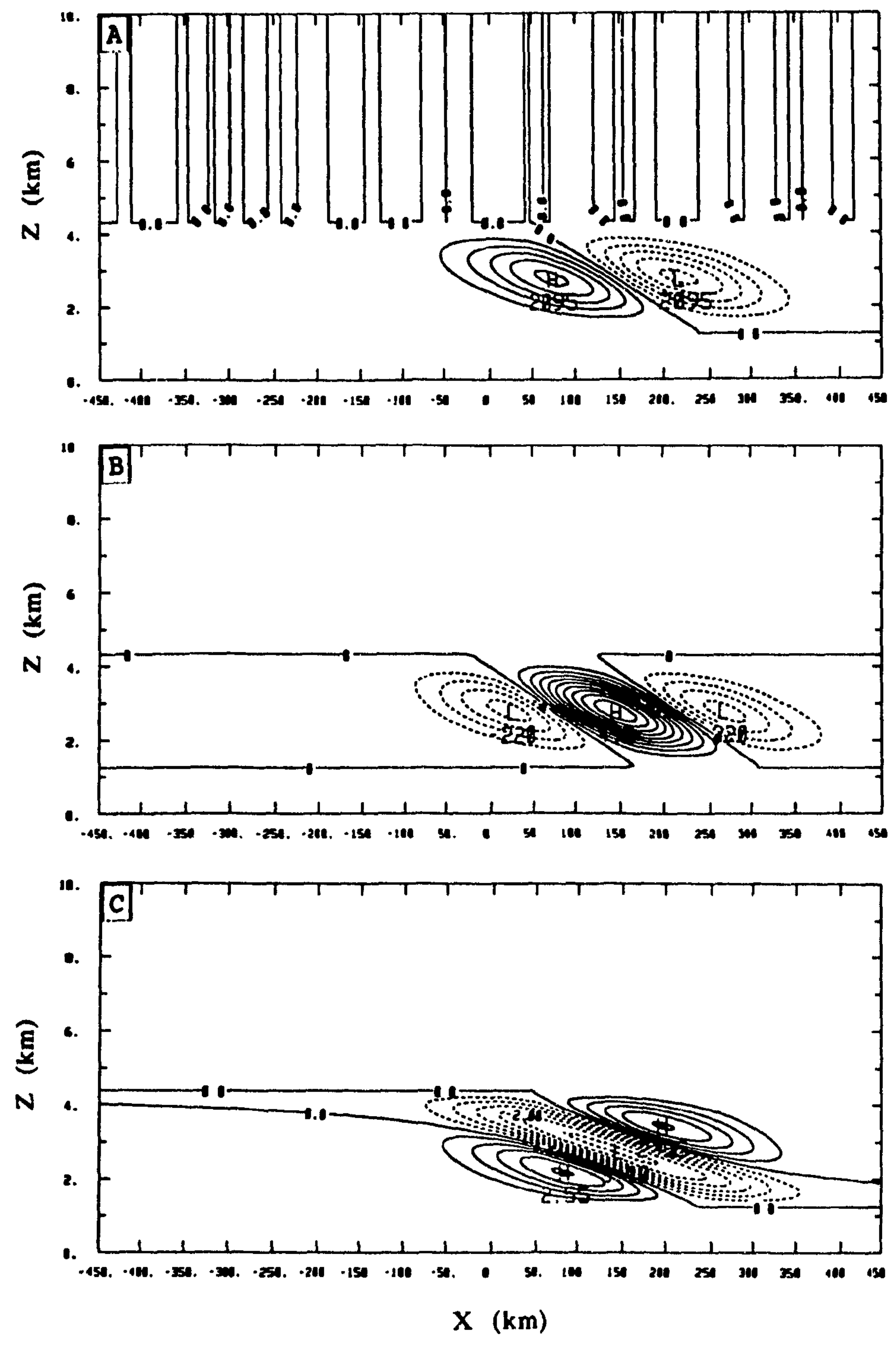

Fig. 3.2. Initial impulse centred at x ≈ 150 km, z ≈ 2.7 km. Negative contours are dashed. (A) Streamfunction. Contour interval is 400 kg m^{-1} s^{-1}. (B) Vertical velocity. Contour interval is 0.005 m s^{-1}. Values shown are scaled by 10000. (C) Velocity in x direction, u′. Contour interval is 0.5 m s^{-1}.

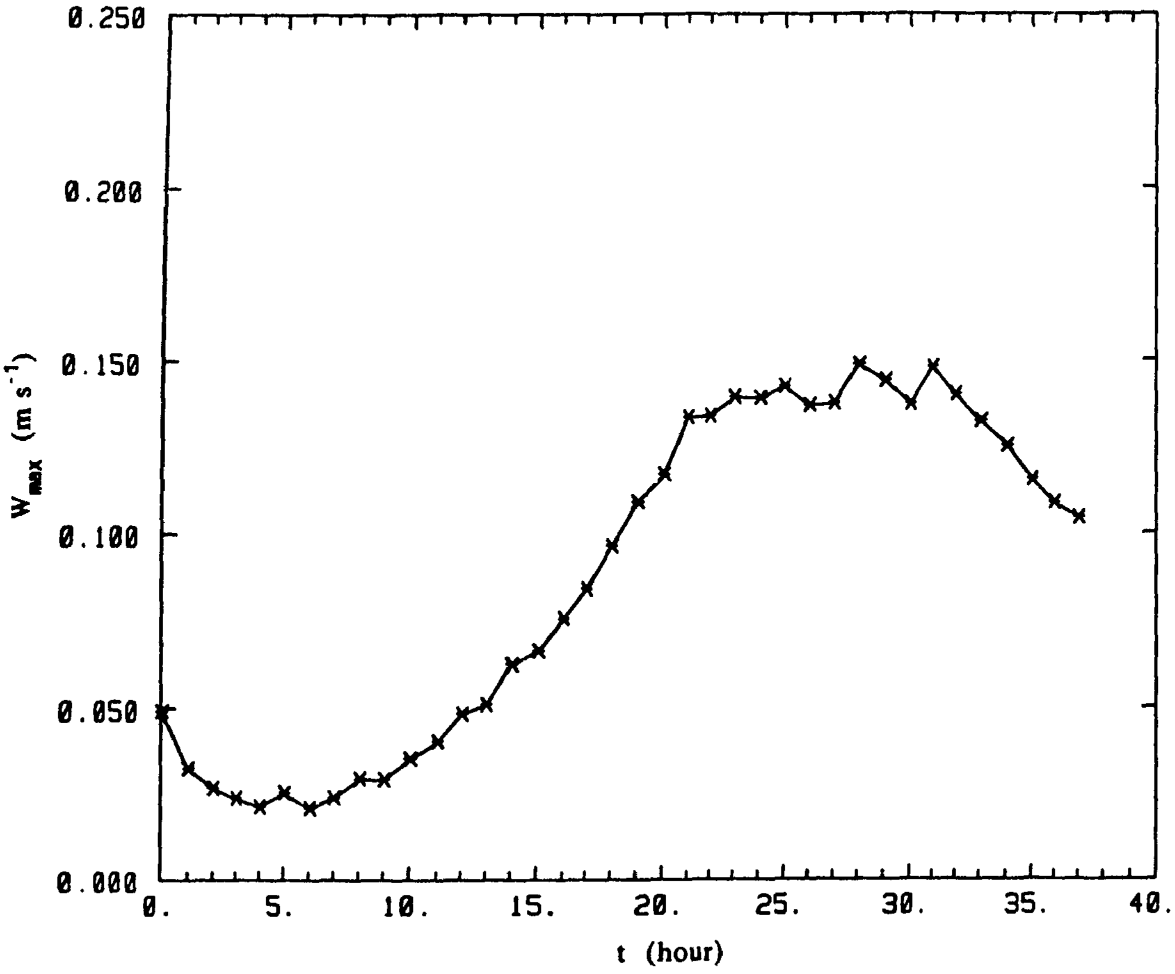

Fig. 3.3. Evolution of maximum vertical velocity in the CSI circulation (unit: m s^{-1}).

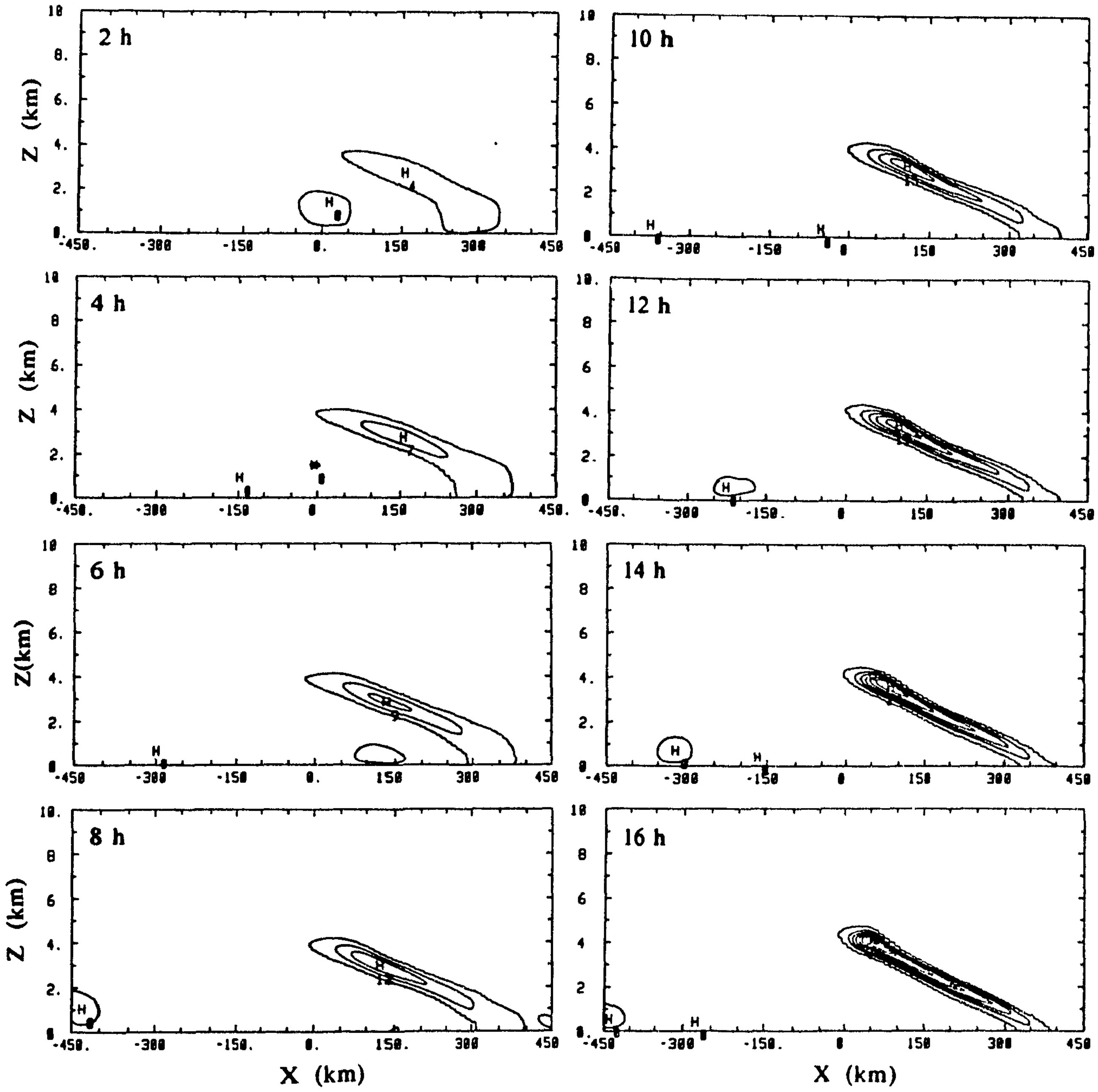

Fig. 3.4. The evolution of cloud water mixing ratio. Cross sections are shown every 2 hours. The first contour is 0.01 g kg^{-1}. Contour interval is 0.4 g kg^{-1}.

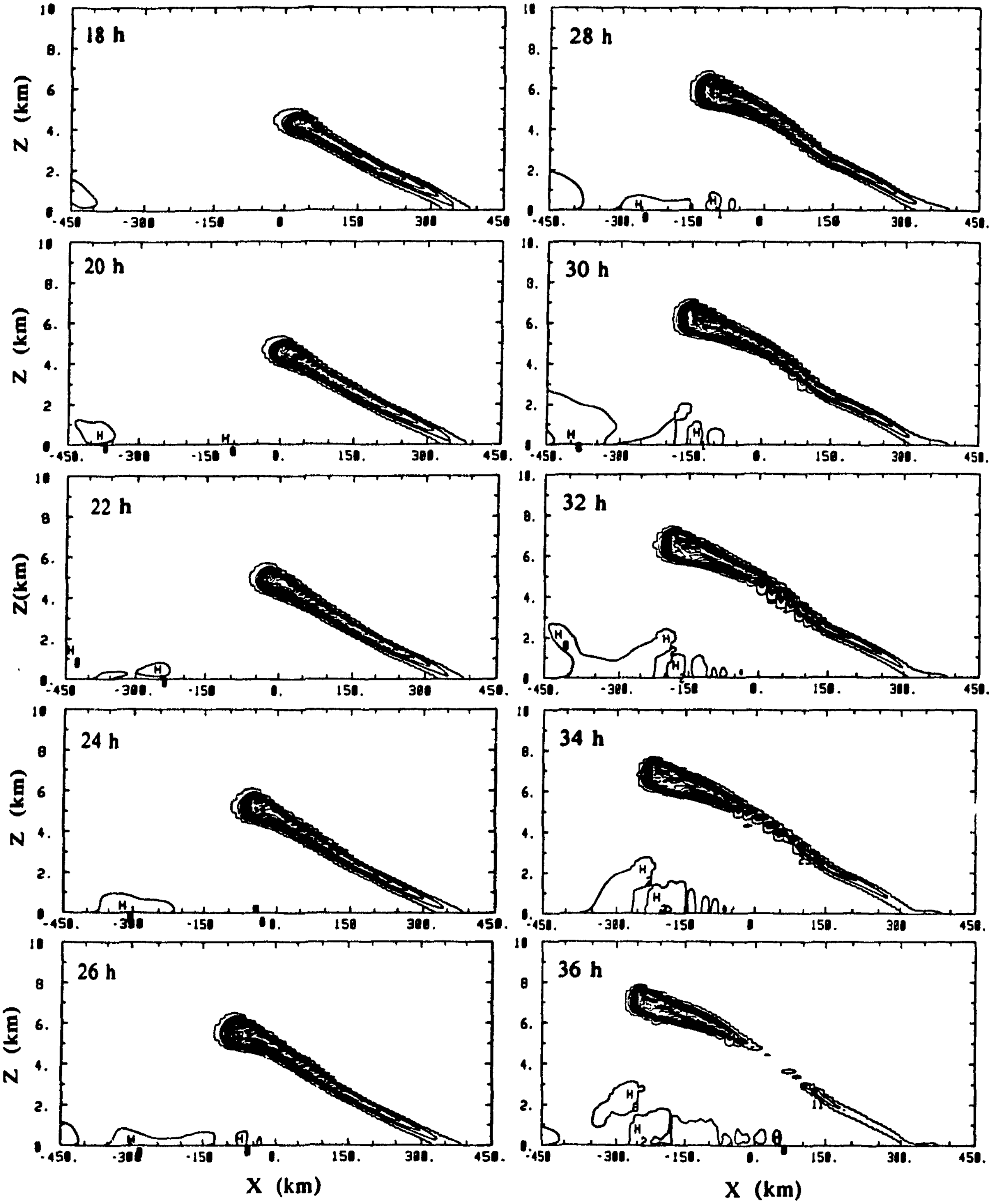

Fig 3.4. (continued)

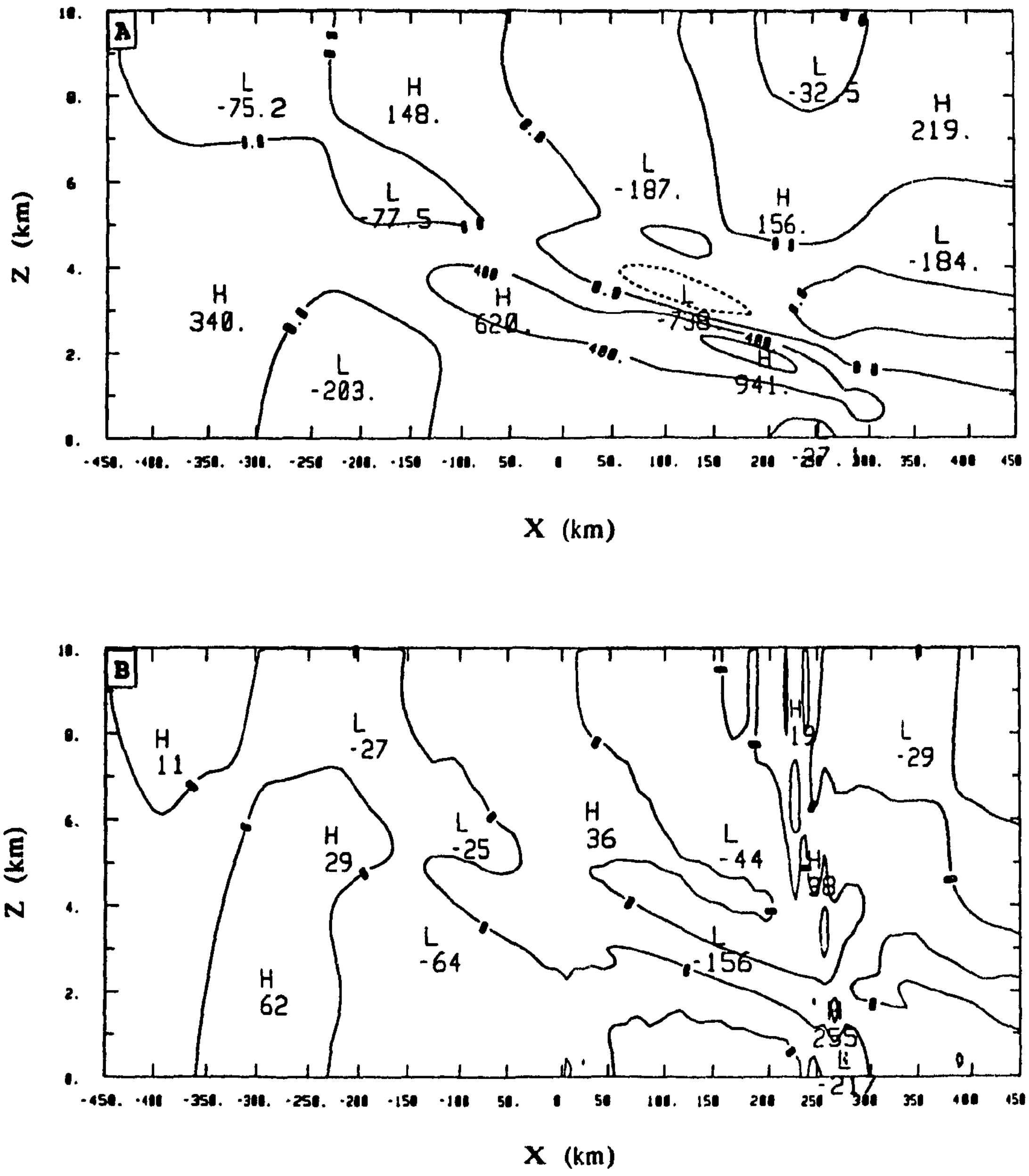

Fig. 3.5. Cross sections of (A) streamfunction (contour interval: 400 kg m^{-1} s^{-1}) and (B) vertical velocity (contour interval: 0.02 m s^{-1}, value scaled by 10^4) at 5 h. Dashed lines correspond to negative values.

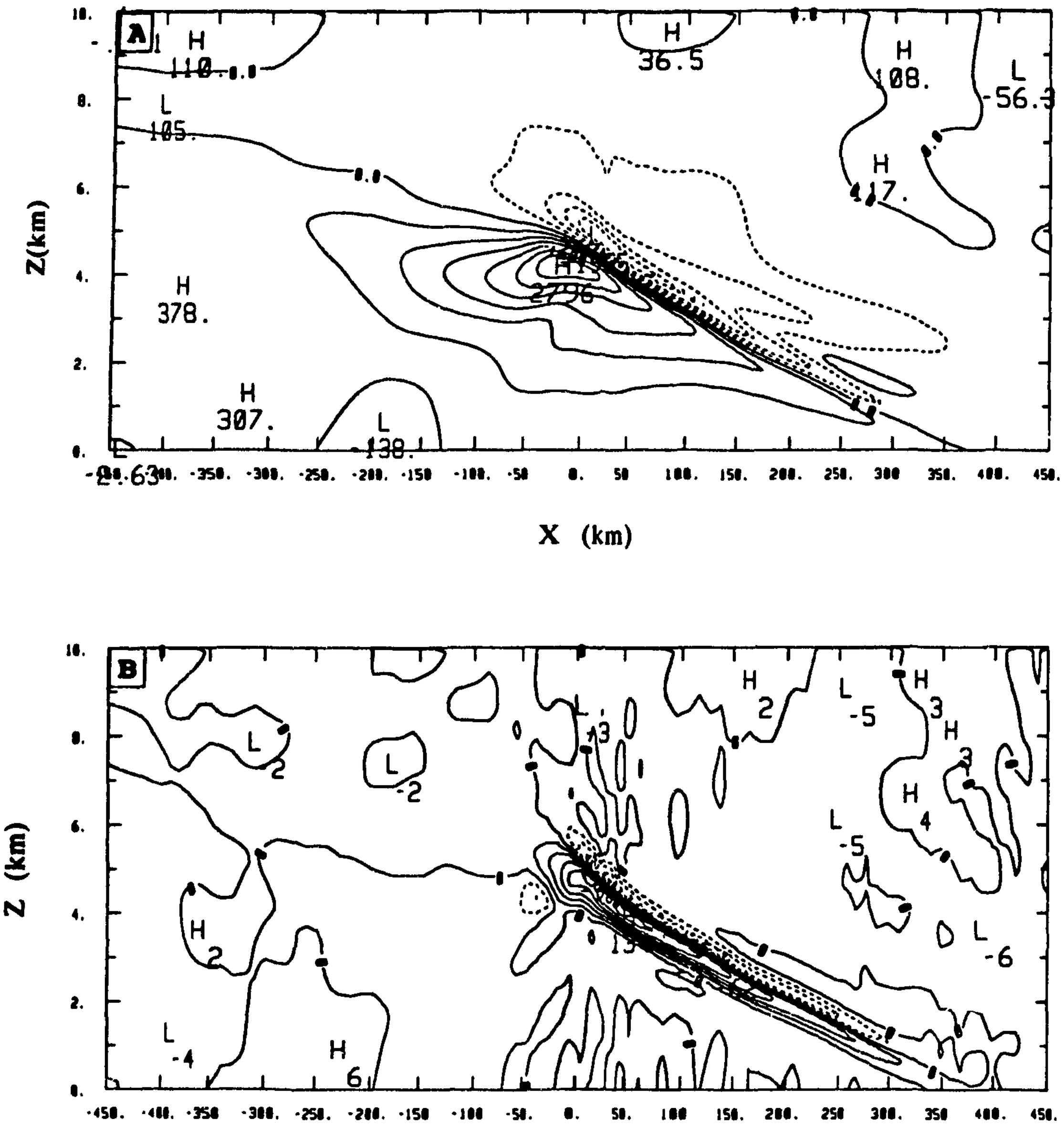

Fig. 3.6. Same as Fig. 3.5, but at 21 h and value of vertical velocity scaled by 1000.

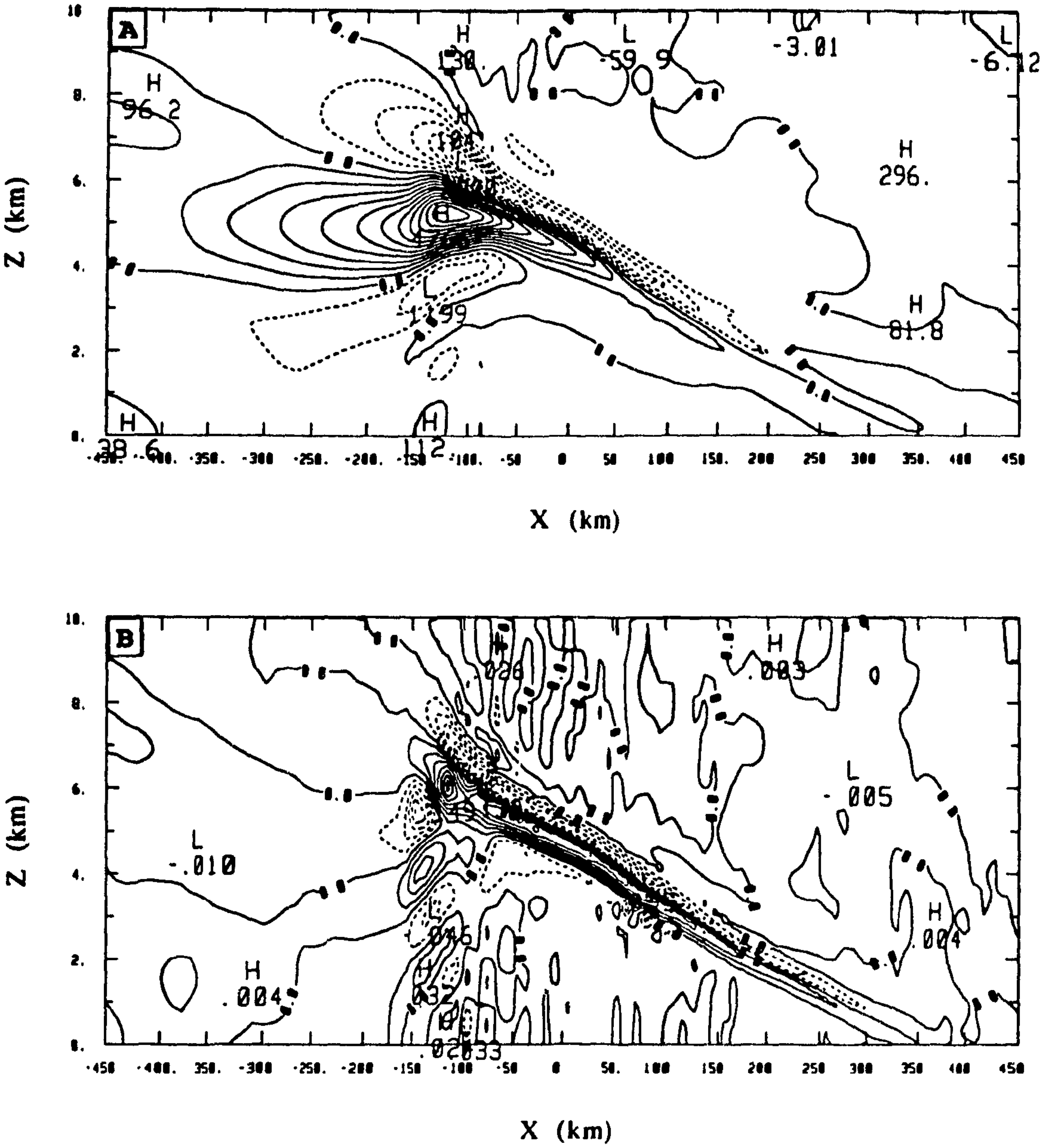

Fig. 3.7. Same as Fig. 3.5, but at 28 h and no scaling.

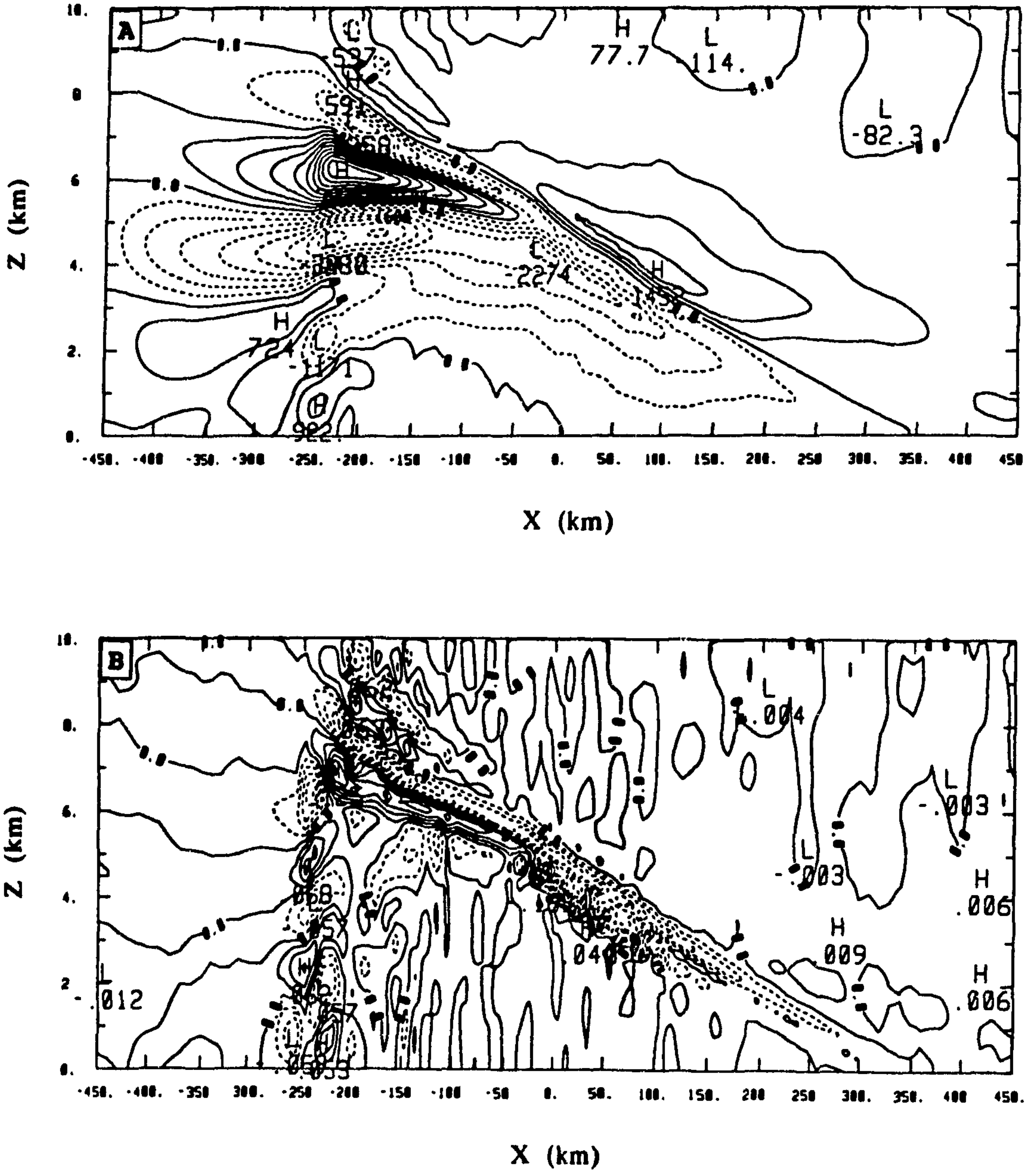

Fig. 3.8. Same as Fig. 3.5, but at 34 h and no scaling.

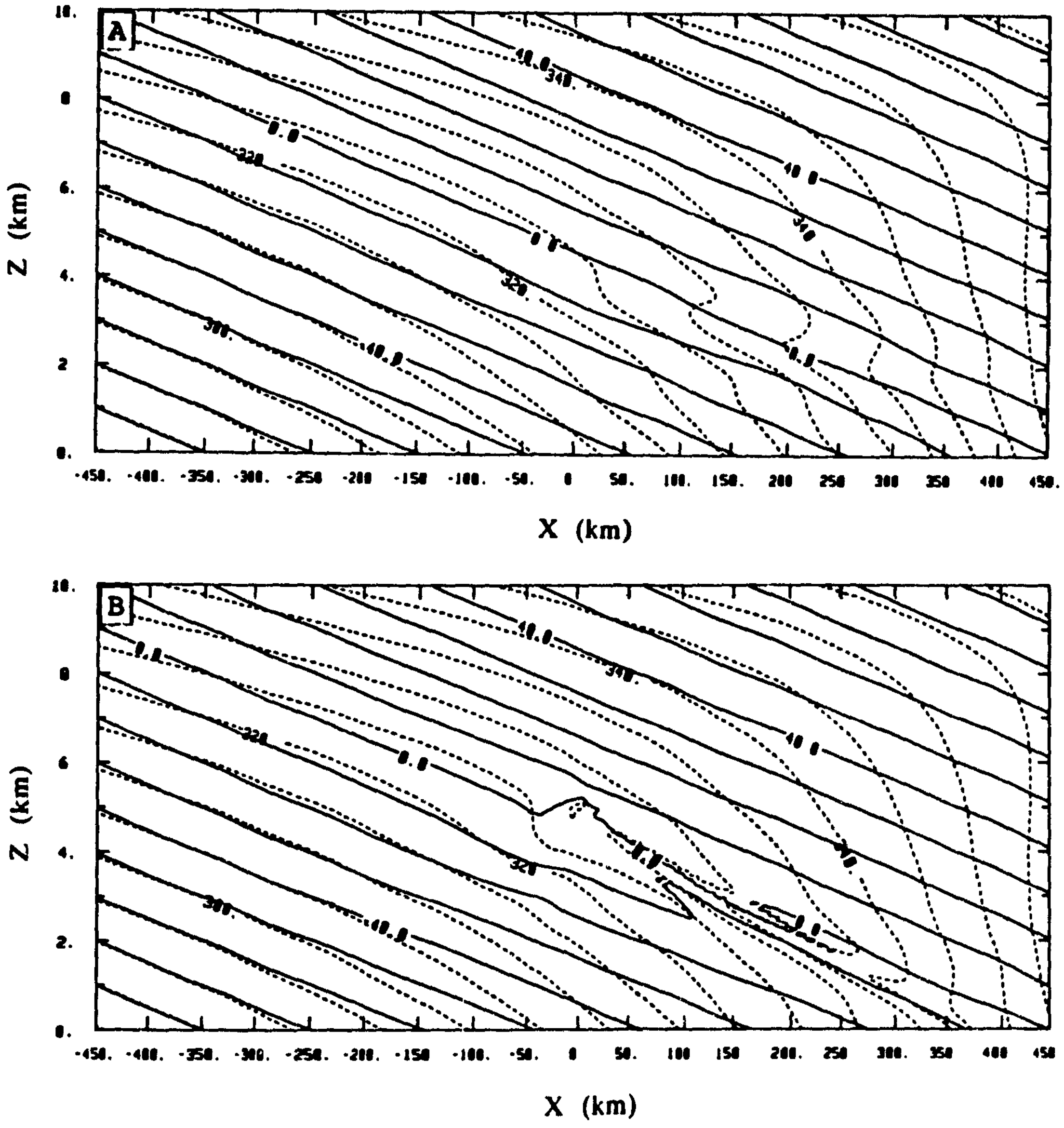

Fig. 3.9. Cross sections of absolute momentum surfaces(solid, contour interval: 10 m s^{-1}) and equivalent potential temperature surfaces(dashed, contour interval: 5 K) at (A) 5 h, (B) 21 h, (C) 28 h and (D) 34 h.

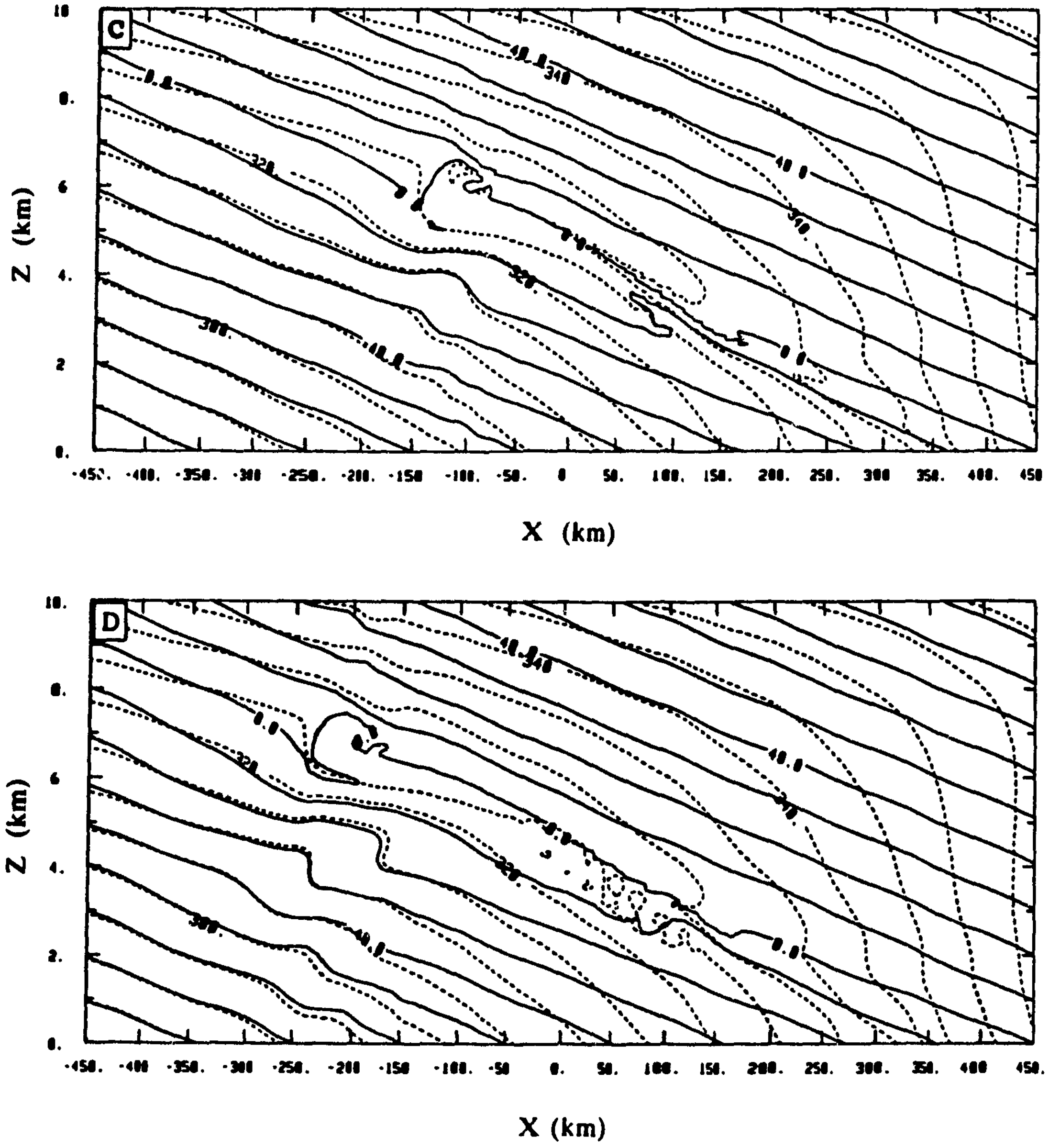

Fig. 3.9. (continued)

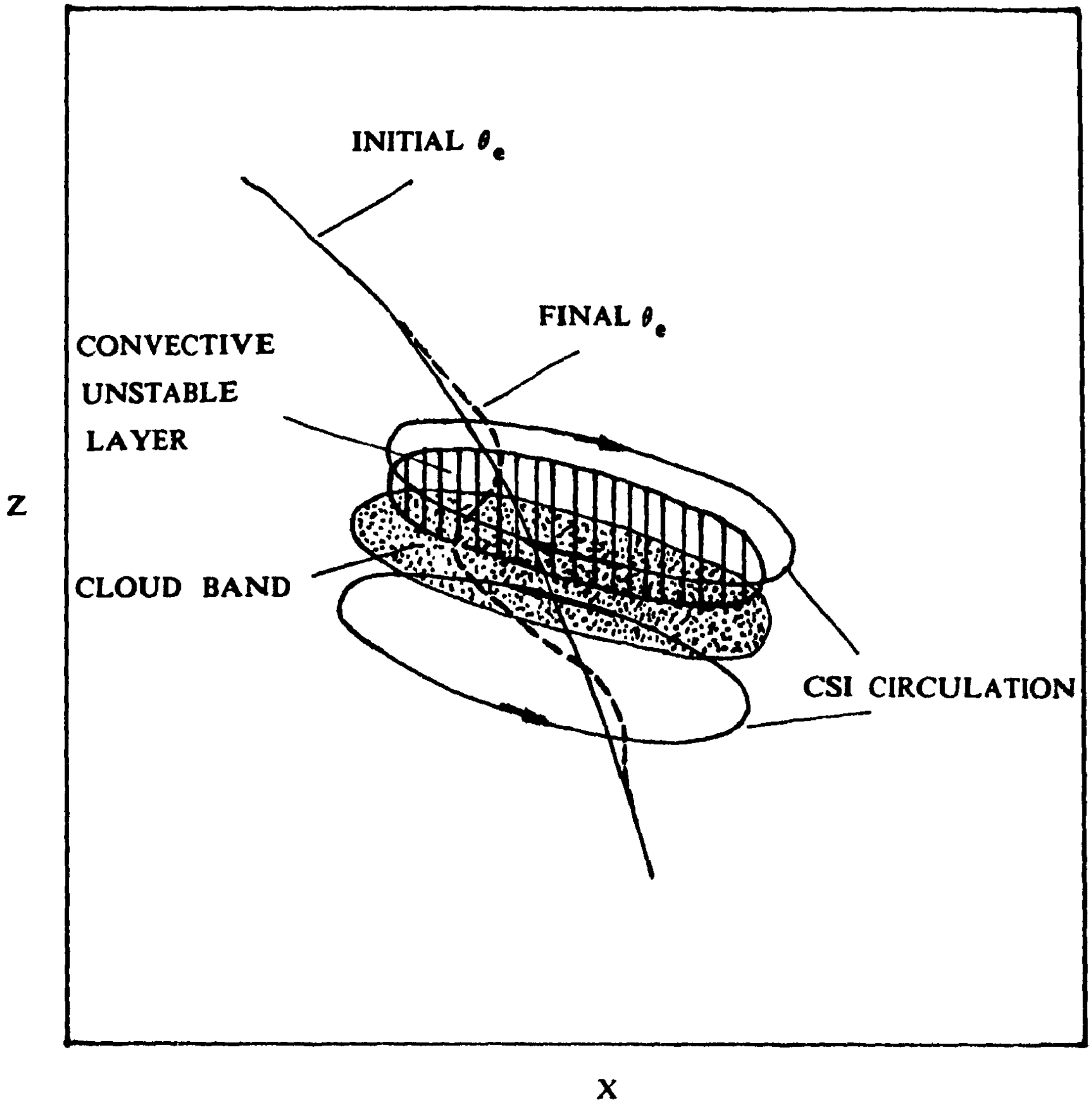

Fig. 3.10. Development of convective instability from the CSI circulation.

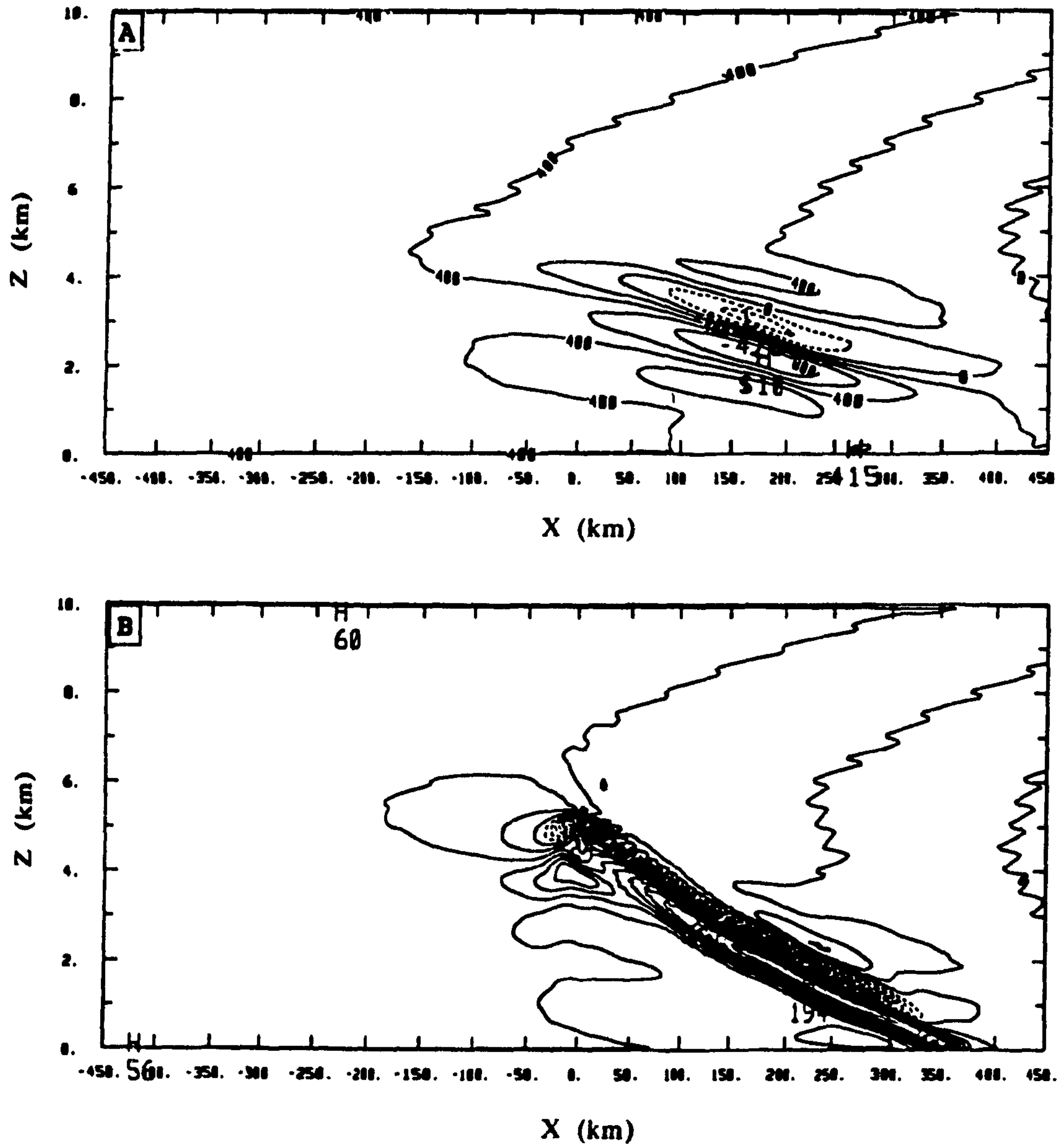

Fig. 3.11(A) Vertical gradient of the equivalent potential temperature at 5 h. Solid and dashed curves show positive and negative contours, respectively. Contour interval is 0.002 K m^{-1}. Values shown in the Figure are scaled by 10^5.

(B) Same as (A) but at 21 h and values scaled by 10^4.

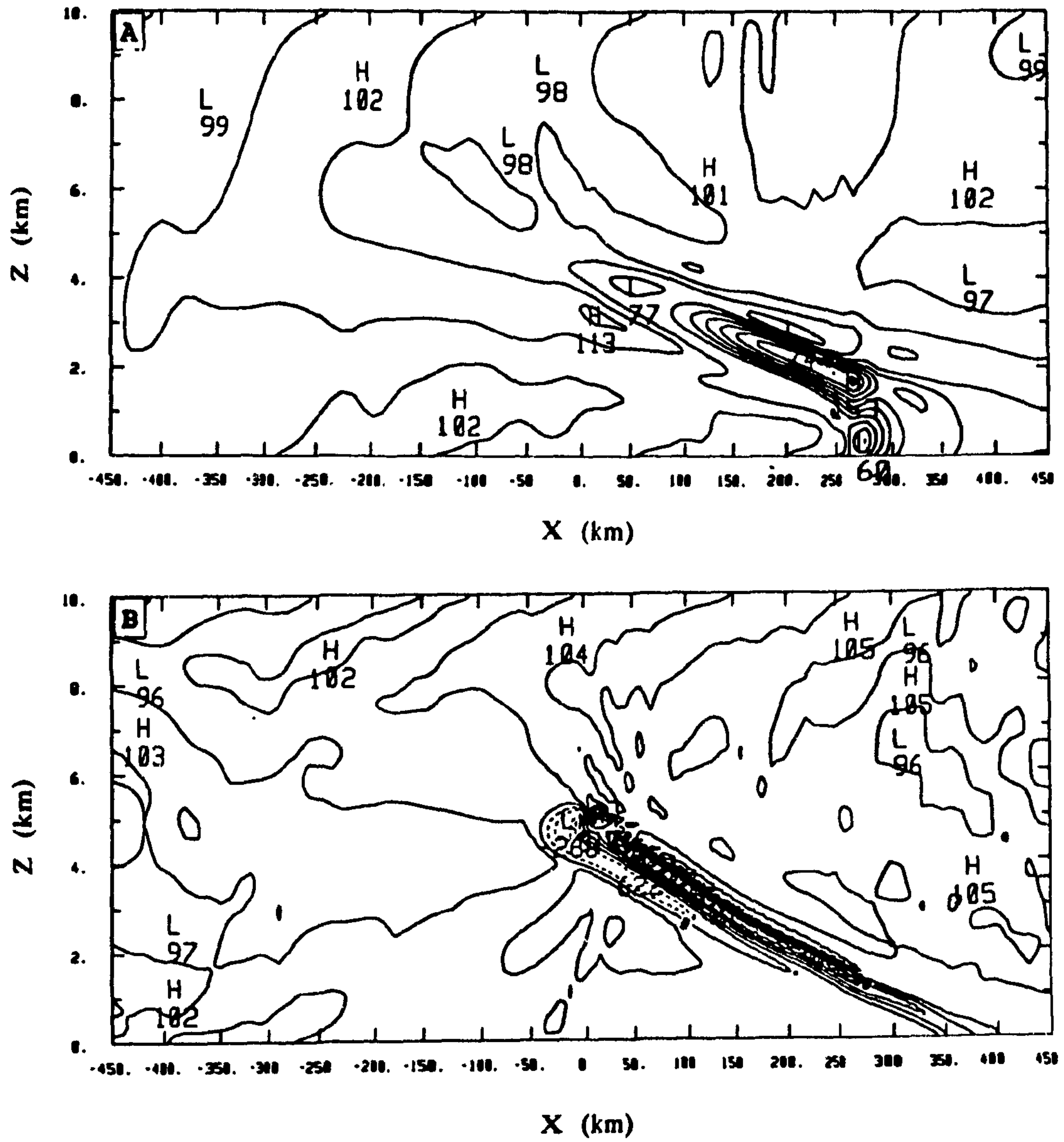

Fig. 3.12(A) Horizontal gradient of absolute momentum at 5 h. Contour interval is 0.00001 m s^{-1}, values shown in the figure are scaled by 10.

(B) Same as (A) but at 21 h and contour interval is 0.0001 .

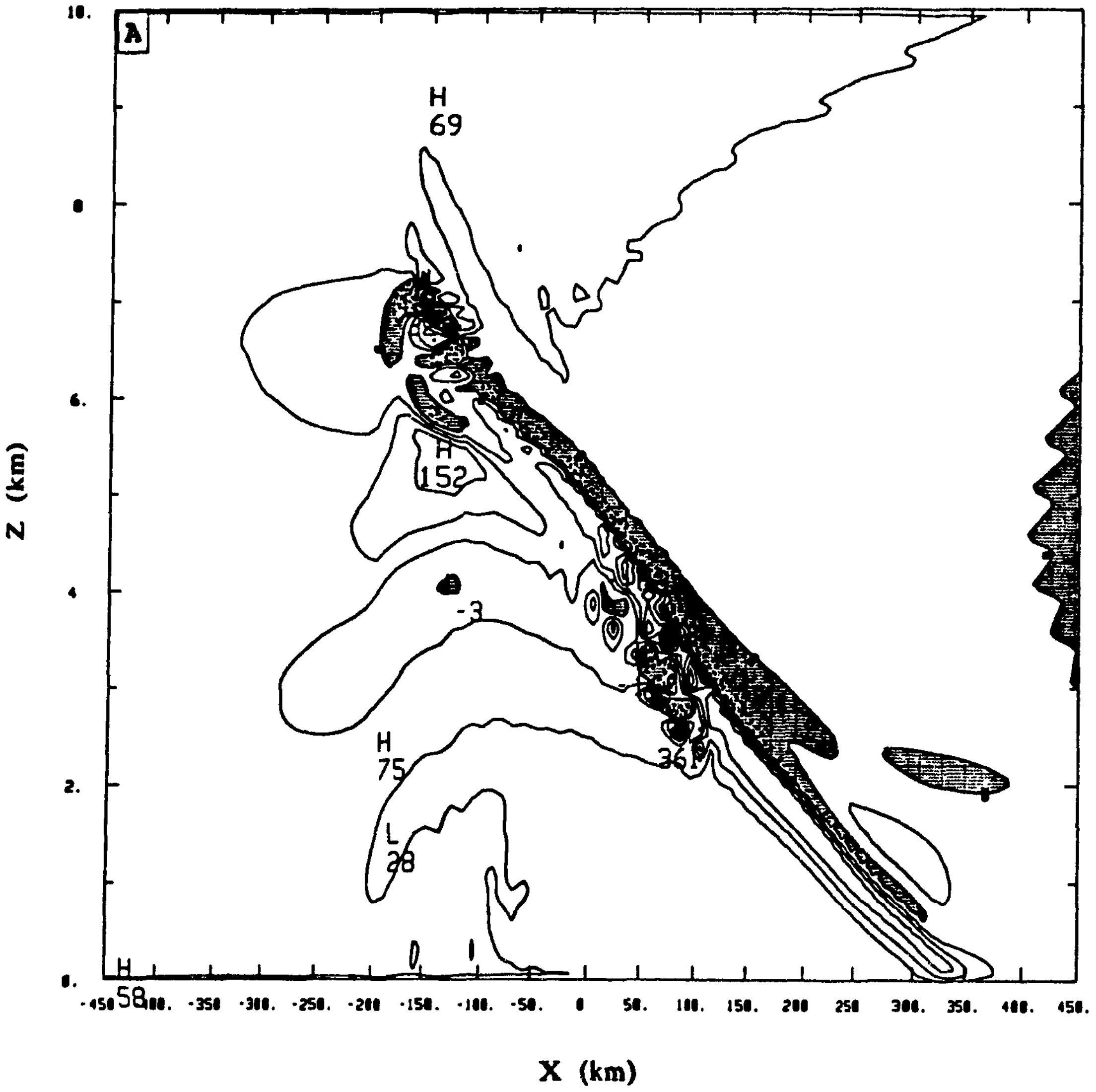

Fig. 3.13 Cross sections of (A) vertical gradient of the equivalent potential temperature (contour interval is 0.004 K m^{-1} and values shown are scaled by 10000), (B) horizontal gradient of absolute momentum (contour interval is 0.00008 m^{-1} and values shown are scaled by 1000000) and (C) cloud water mixing ratio (the first contour is 0.01 g kg^{-1} and contour interval is 0.4 g kg^{-1}) at t=31 h. Areas with negative values are shaded.

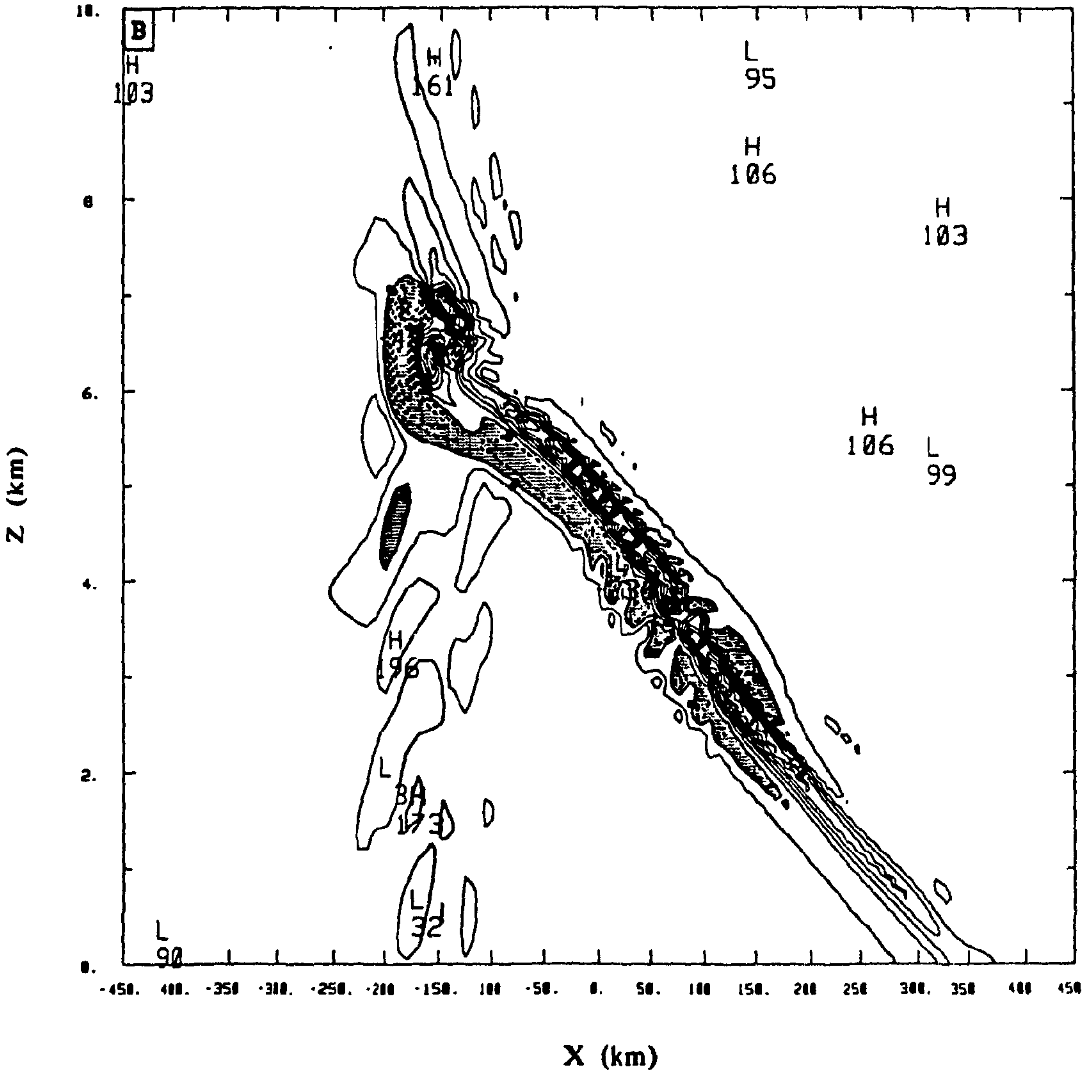

Fig 3.13. (continued)

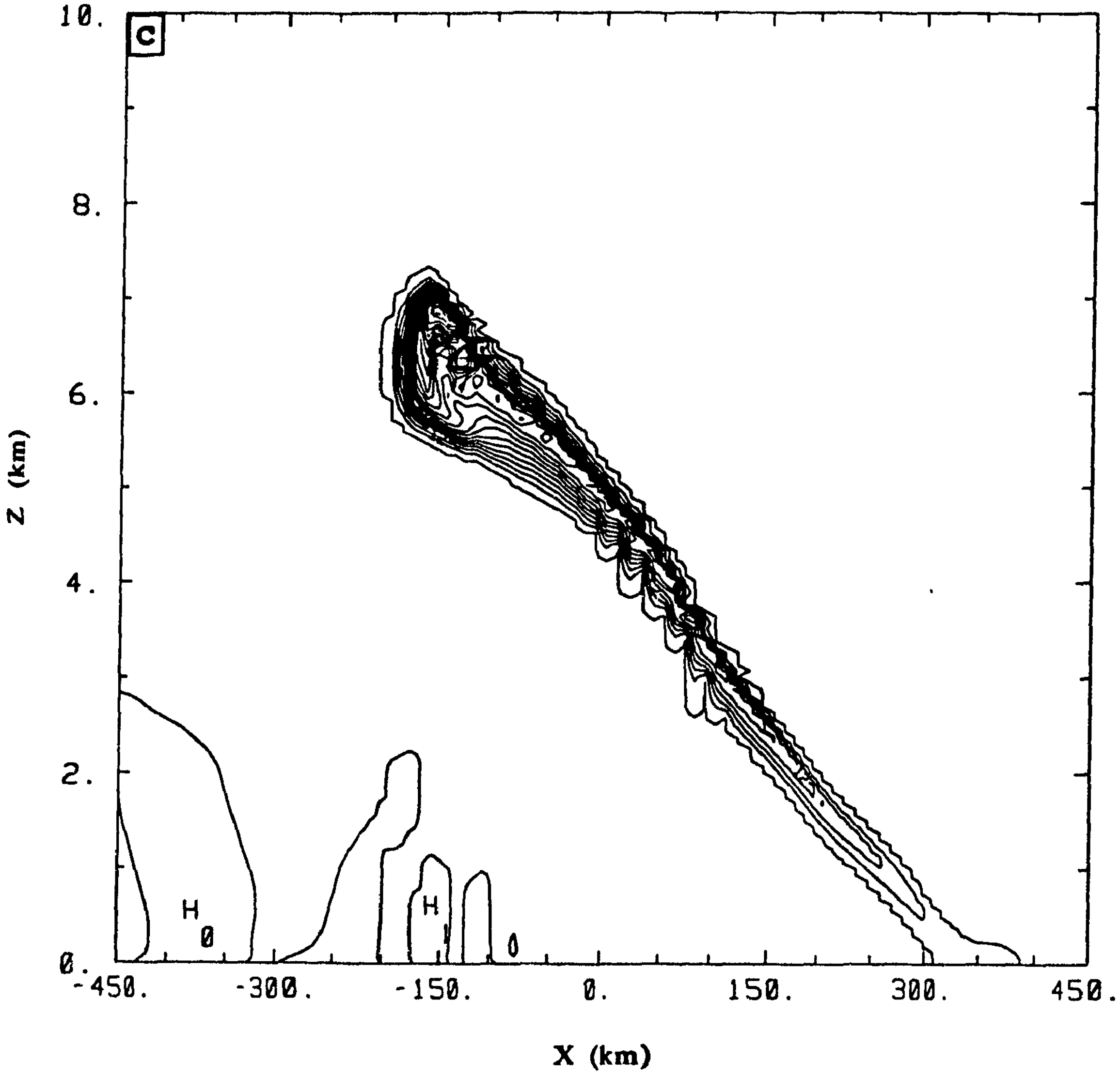

Fig 3.13. (continued)

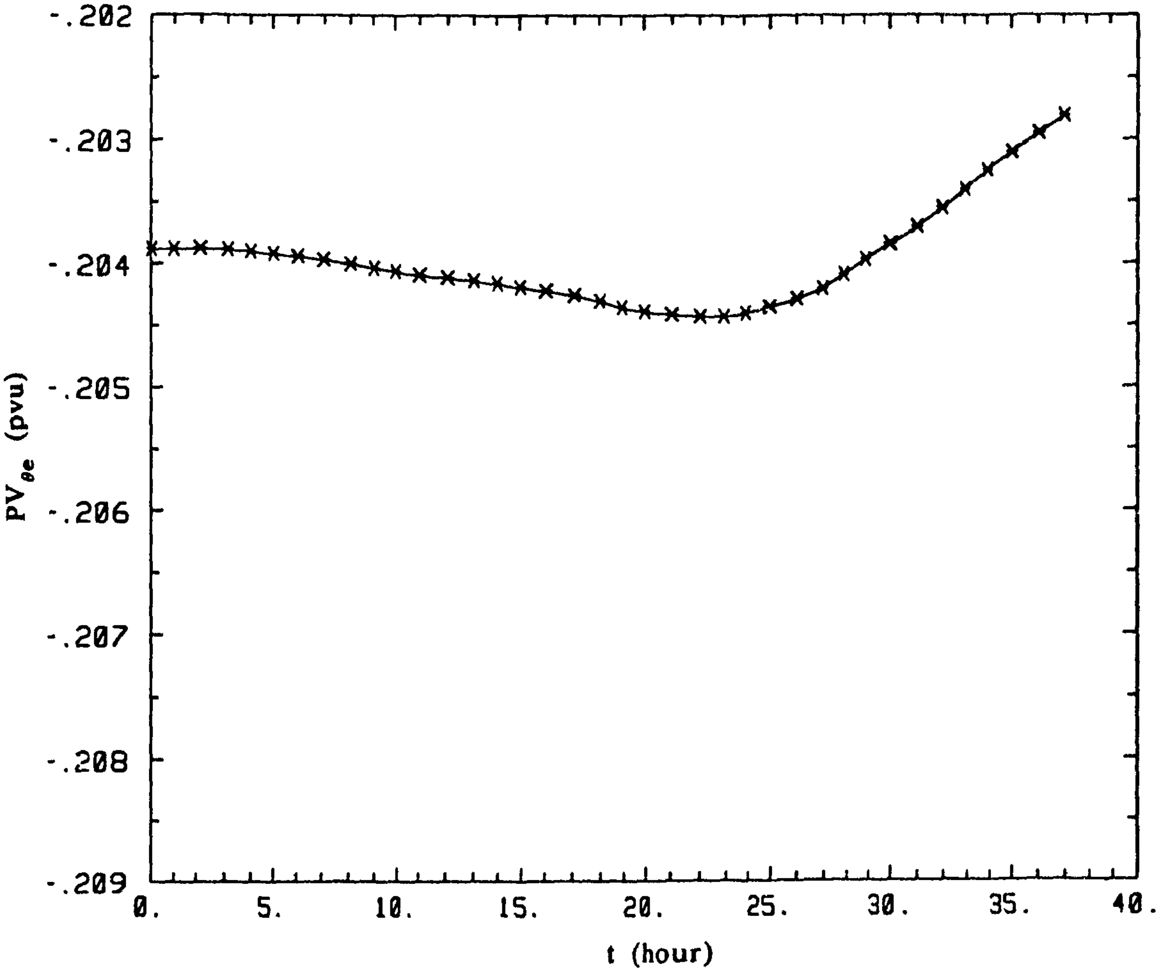

Fig. 3.14. The evolution of domain average equivalent potential vorticity (unit: pvu).

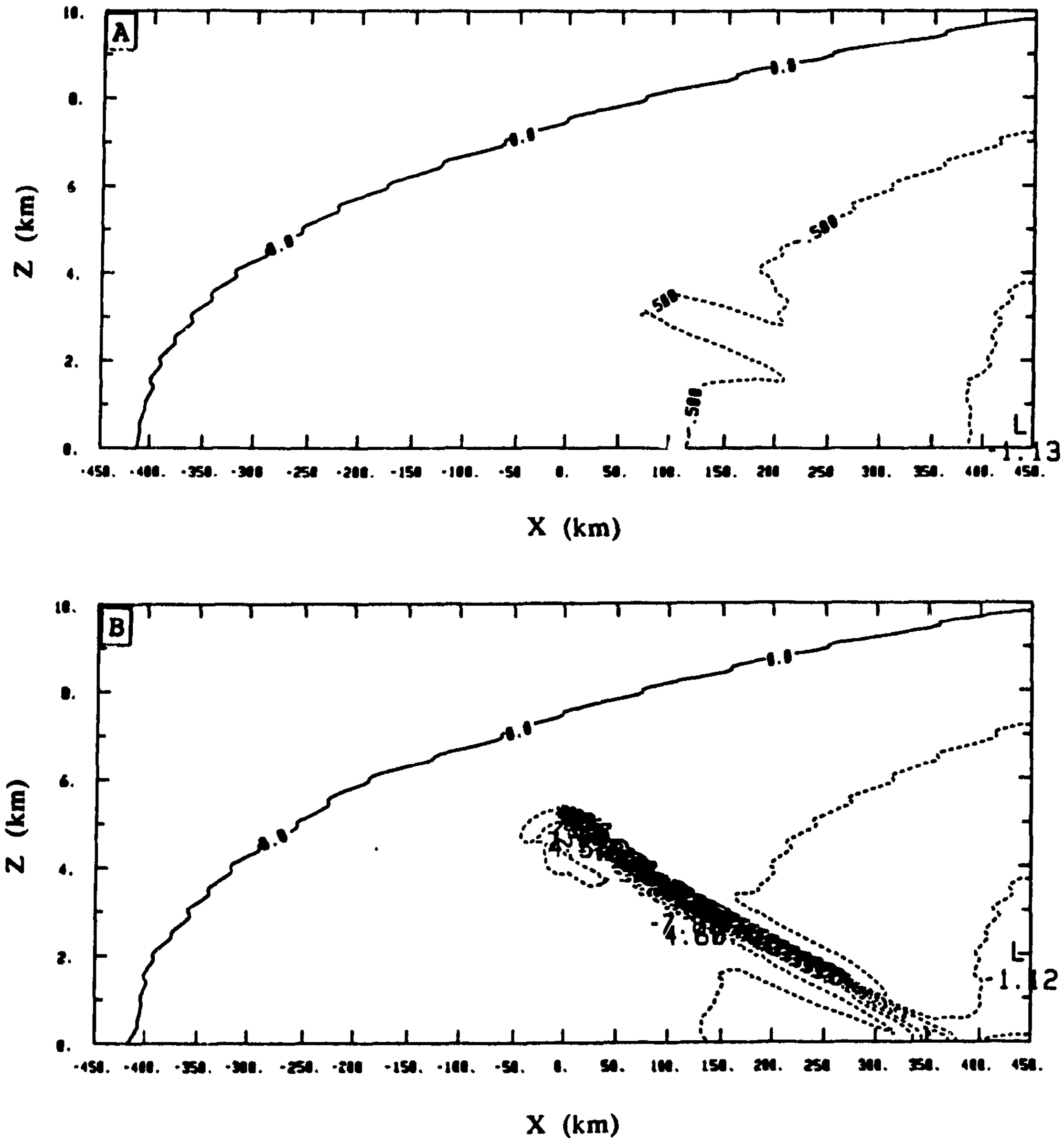

Fig. 3.15. Cross sections of equivalent potential vorticity at (A) 5 h, (B) 21 h, (C) 28 h and (D) 34 h. Contour interval is 0.5 pvu. Dashed lines show negtive values.

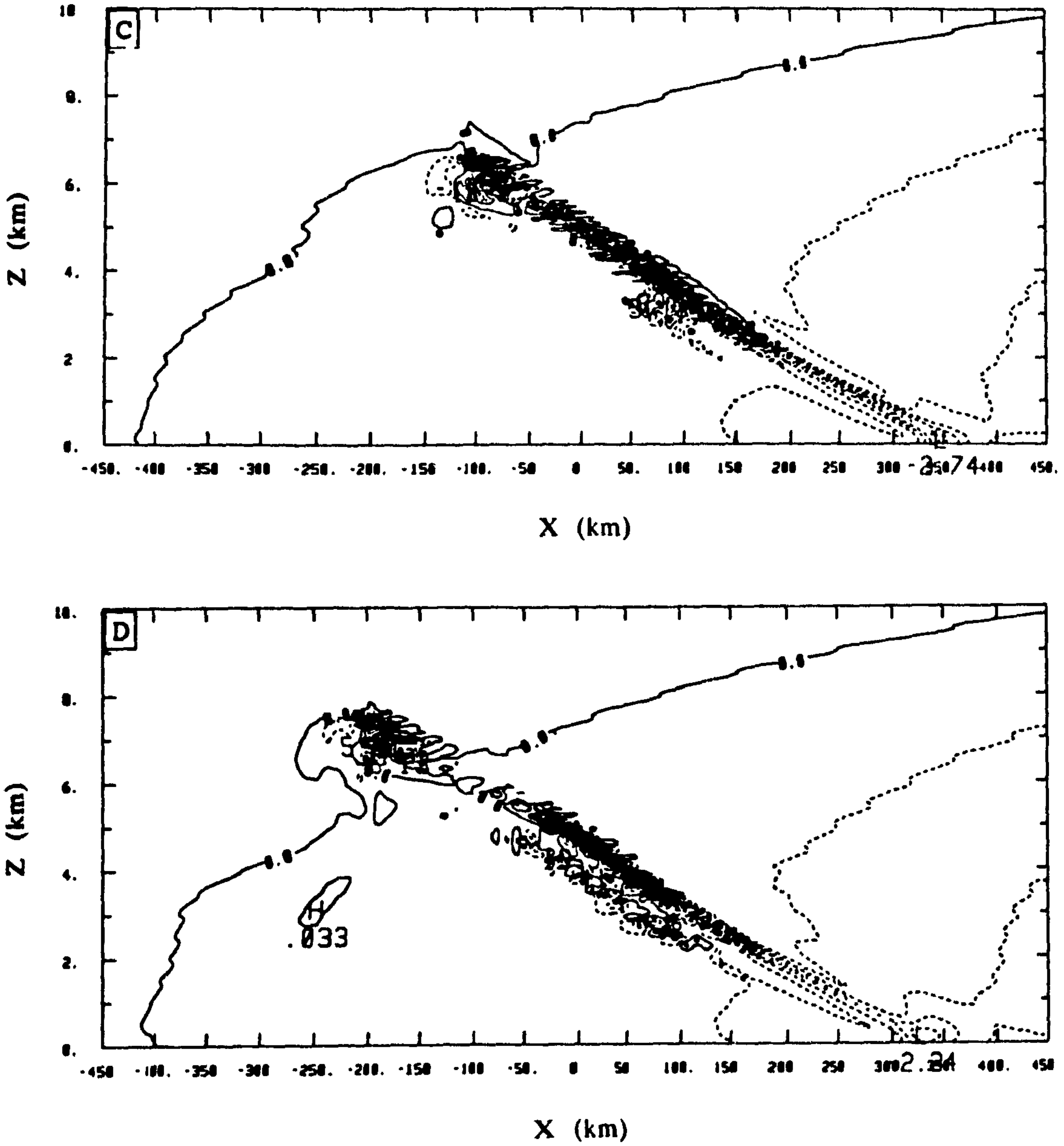

Fig 3.15. (continued)

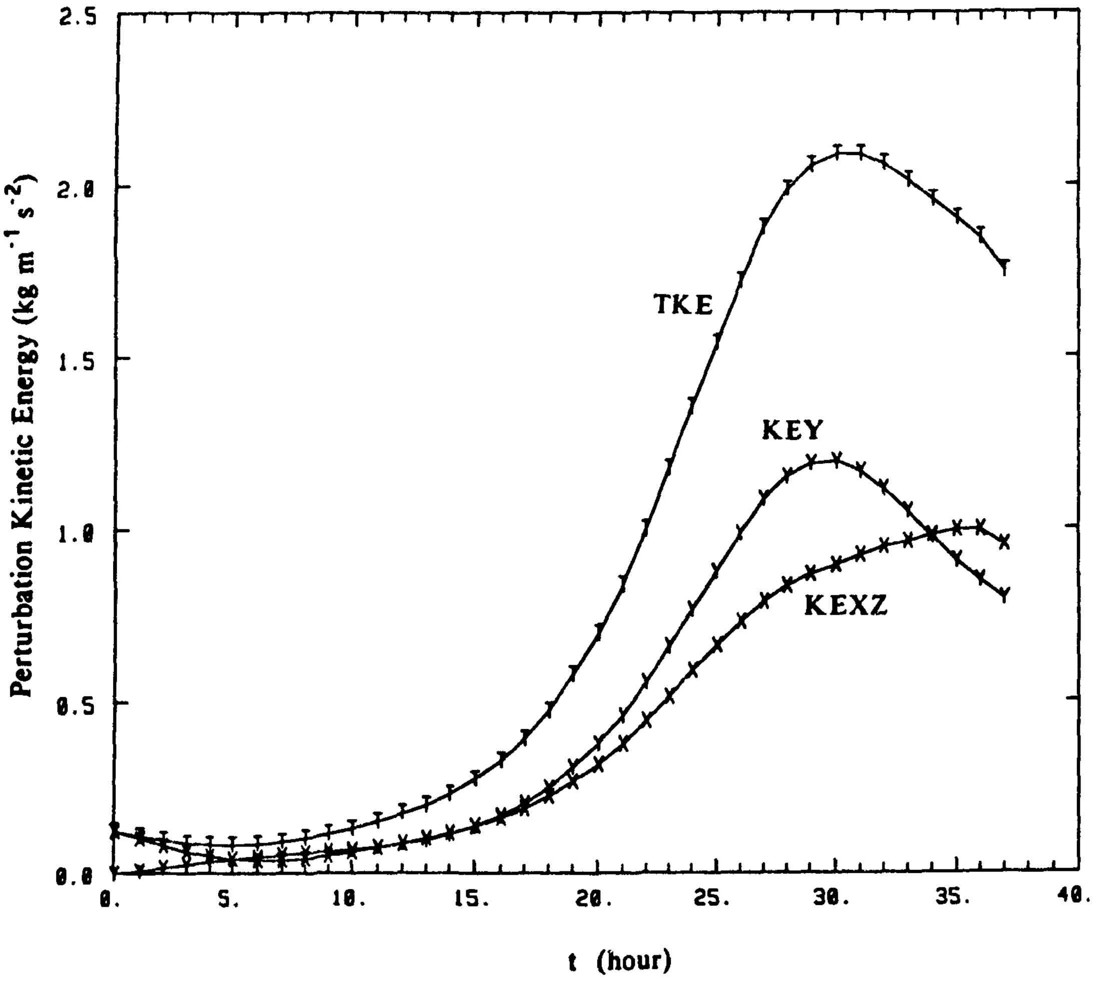

Fig. 3.16. Evolutions of total perturbation kinetic energy (TKE), along-band (y direction) perturbation kinetic energy (KEY) and transverse perturbation kinetic energy (KEXZ).

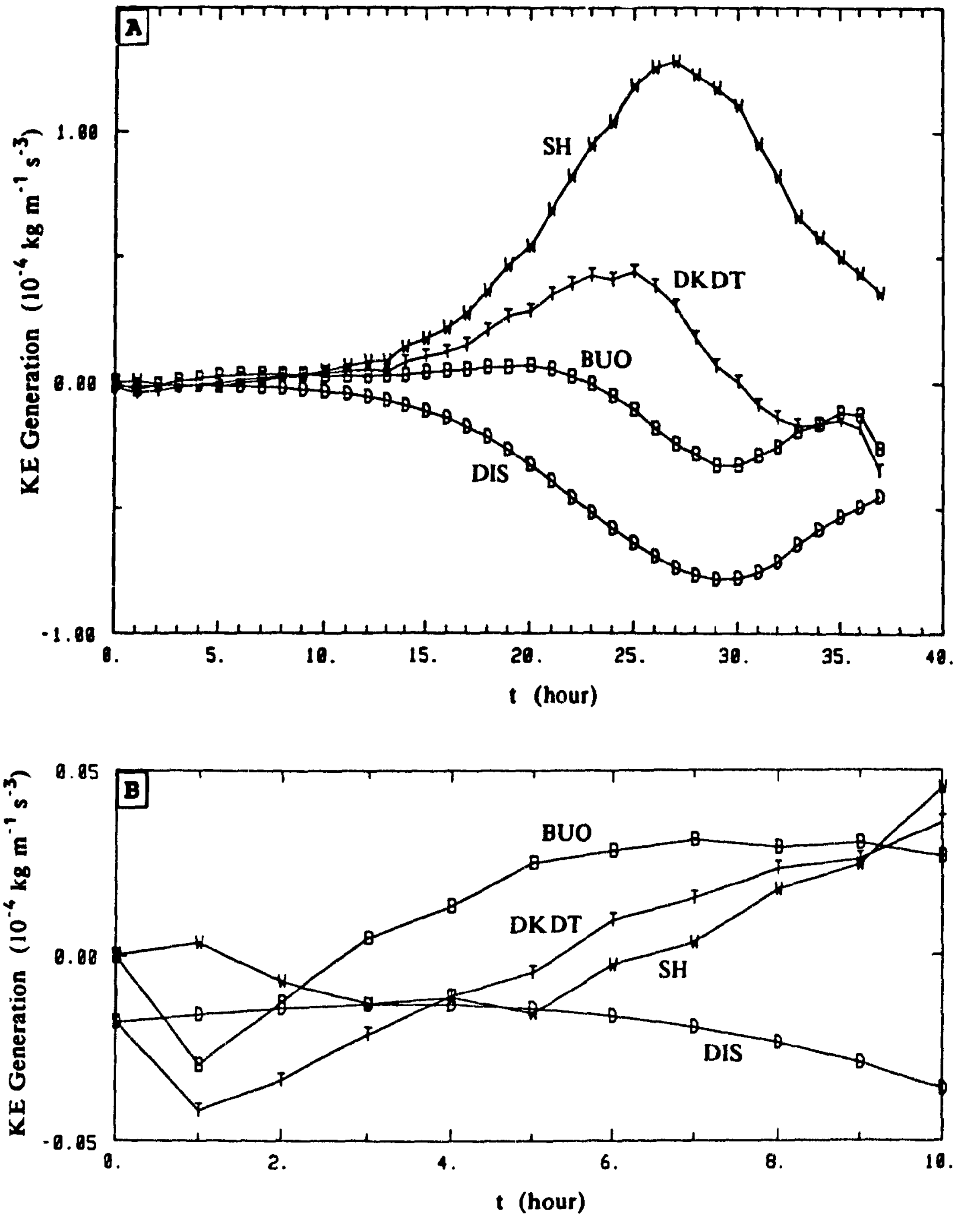

Fig. 3.17. Time change rate of perturbation kinetic energy and its contributors as a function of time, during (A) whole 37 h simulation, (B) first 10 h simulation. (see text for more details)

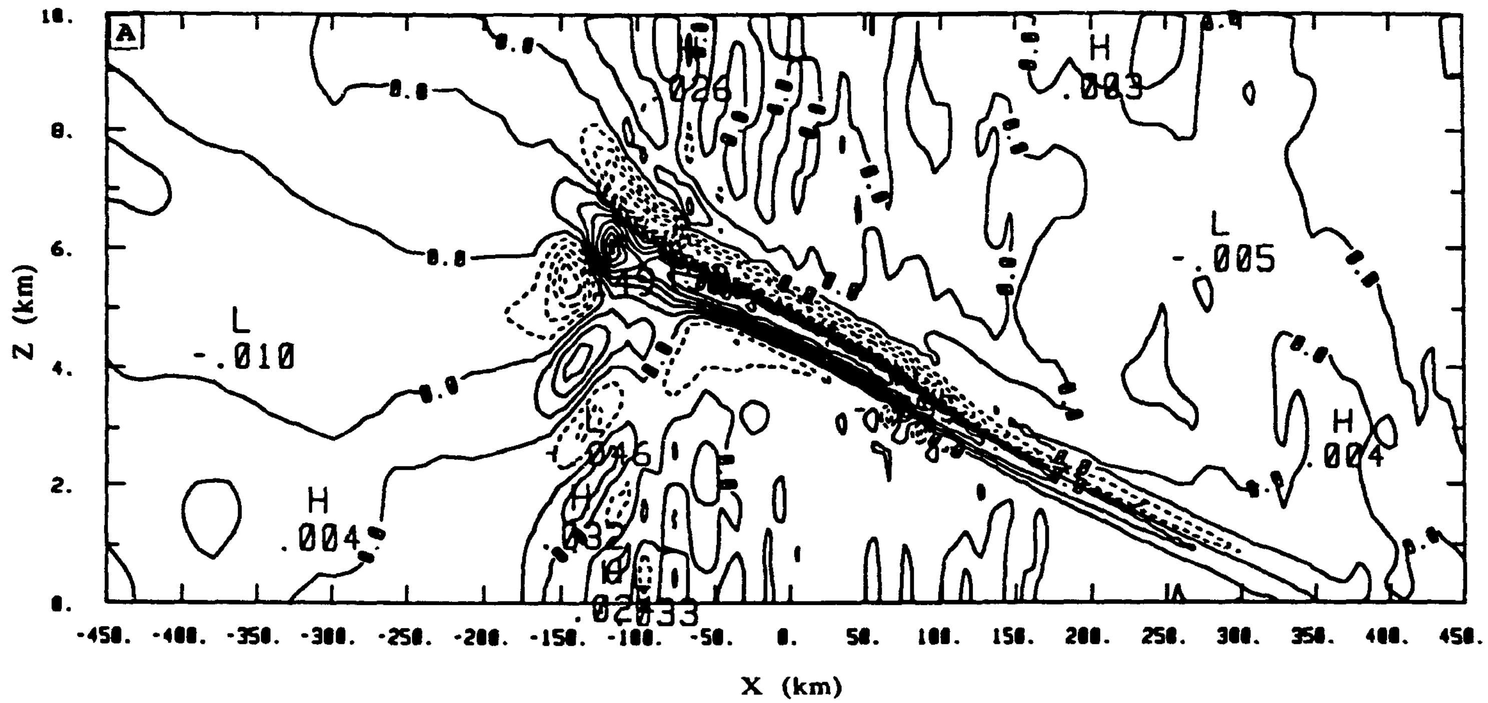

Fig. 3.18. Cross sections of vertical velocity for (A) simulation L160; (B) simulation L80 and (C) simulation L40 at t = 28 h. Contour interval is 0.02 m s^{-1}.

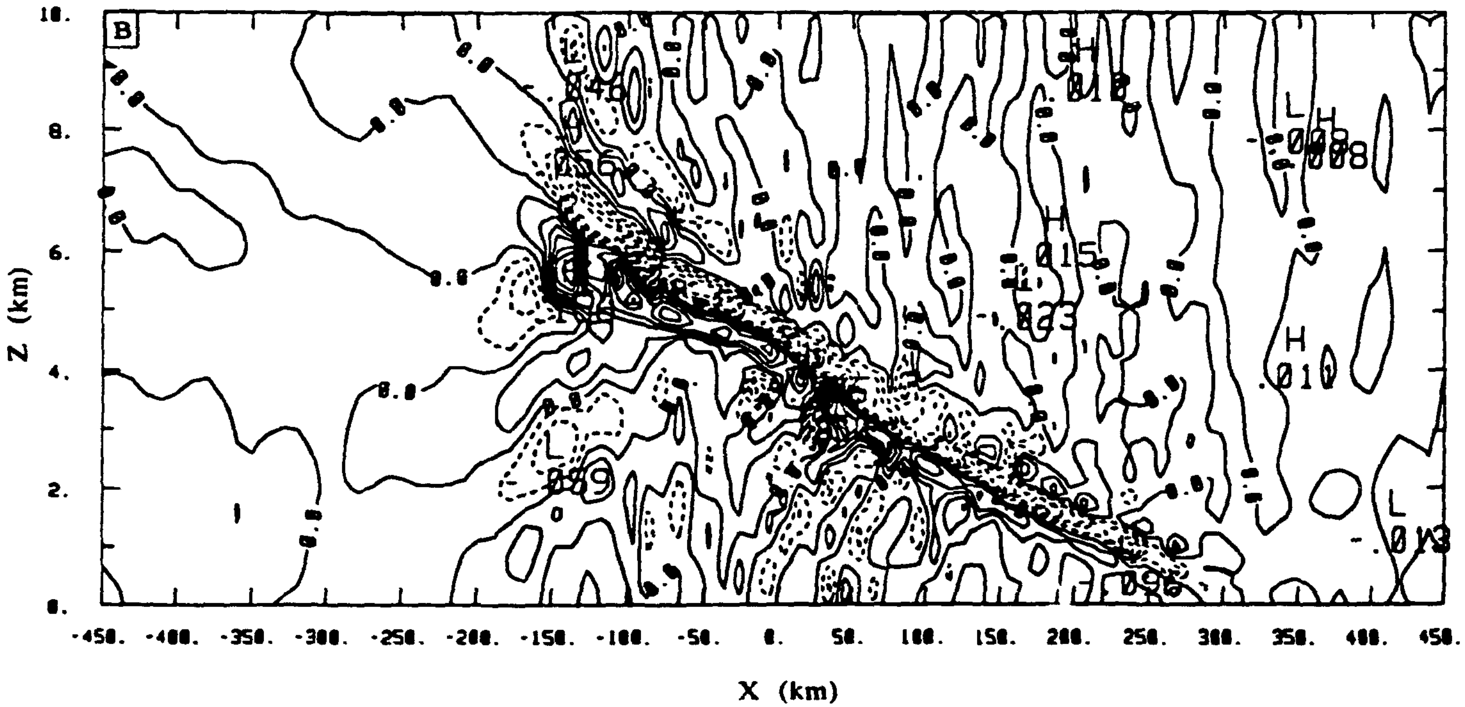

Fig 3.18. (continued)

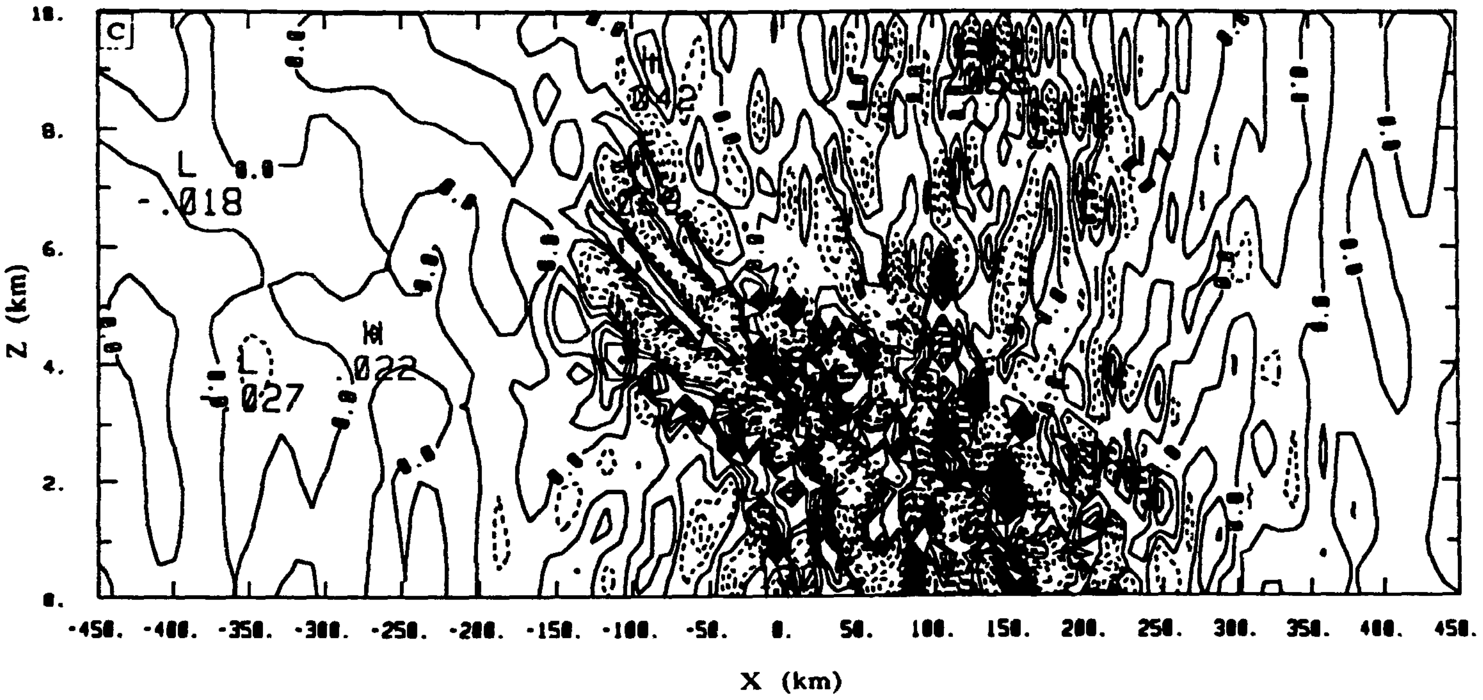

Fig 3.18. (continued)

CHAPTER 4

SUMMARY AND CONCLUDING REMARK

A life-cycle of slantwise convection has been simulated. Many features of the circulation of CSI are similar to those predicted by linear theory and other modelling studies. It can be concluded that this modified model is suitable for the simulation of slantwise convection and for the study of the evolution of CSI.

The simulated cloudband goes through a life-cycle which can be divided into four stages, namely onset, growth, mature and decay. The key features of each stage can be summarized as follows.

Onset stage (0 - 6 h): The amount of condensation is relatively small. Although the area with low value of $PV_{\theta e}$ has extended along the updraft, the initial impulse has weakened considerably, the maximum vertical velocity decreases from 4.9 cm s^{-1} to 2.55 cm s^{-1}. Negative buoyancy and dissipation are together responsible for the initial decrease of perturbation kinetic energy.

Growth stage (6 - 25 h): A well-defined CSI circulation has formed. The stream function shows a very narrow, slanted updraft. The axis of the updraft appears to be more horizontal than that at initial time, although it still lies between the M and θ_e surfaces. The maximum vertical velocity increase rapidly and reaches 13.4 cm s^{-1} at 21 h. A strong and very narrow downdraft is located immediately above the updraft. The cloud band develops quickly during this stage. The location of the band coincides with that of the narrow, sloping updraft in the CSI circulation. M and θ_e surfaces undergo significant deformation in the region of the CSI circulation. Both convectively and inertially unstable layers resulting from the advection of

M and θ_e surfaces by the circulation can be observed. While the domain averaged $PV_{\theta e}$ increases (becomes less negative) slowly, the positive and negative $PV_{\theta e}$ anomalies produced by the turbulent diffusion can also be observed. During this stage the shear generation term in the equation of time rate of change of perturbation kinetic energy increases greatly, resulting in the net generation of perturbation kinetic energy.

Mature stage (25 - 31 h): The updraft of the CSI circulation has extended to an altitude of 8 km. The maximum vertical velocity in the circulation reaches 15 cm s^{-1} and stops increasing. The downdraft begins to develop at the lower portion of the cloud band. Vertical convective cells can be found in the cloudband. In the energetics, stronger negative buoyancy and increasing dissipation cause the decrease of the perturbation kinetic energy.

Decay stage (31 - 37 h): The strength and the extent of the circulation and the maximum vertical velocity decrease considerably. Downdraft develops continuously at the lower portion of the band. The cloud there dissipates gradually. However, the upper portion of the cloudband continues to persist. The convective and inertial instability induced by the circulation have weakened greatly, but in contrast the low values of $PV_{\theta e}$ have been advected into the region previously stable to slantwise and upright convection. The energy analysis also shows a smooth decrease of perturbation kinetic energy.

During the simulation some interesting features of the CSI circulation have been noted. The convectively and inertially unstable layers can be induced as the results of the advections of M and θ_e surfaces by the updraft and downdraft of the CSI circulation. While the convectively unstable region mainly develops near the top of the band, areas of inertial instability can be located near both the top and the bottom of the cloud. The convective cells can be observed in the cloudband.

Our results show that the main source of perturbation kinetic energy of the CSI circulation is the basic flow in the form of vertical shear. In contrast, the dissipation (turbulence) always acts as an energy sink. The buoyancy makes a positive contribution during the growth stage and a negative one during the mature and decay stages.

It is found that at the end of the simulation, although the maximum vertical velocity and perturbation kinetic energy indicate the onset of the decay stage, the neutral state ($PV_{\theta e} \approx 0$) has not been achieved. The positive and negative $PV_{\theta e}$ anomalies persist with no sign of being removed.

Consistent with the vertical resolution estimate by Persson and Warner(1991), our results show that if a horizontal grid length of 10 km is used in the simulation of CSI, a high vertical resolution (more than 80 layers) should be used to avoid spurious gravity waves.

We believe that the most important improvement in future work would be to include precipitation processes into the model. It will eliminate the large accumulation of cloud water in the cloudband. The incorporation of evaporation and ice physics should improve the simulation of the decay stage. Turbulence appears to be a very important factor for the evolution of conditional symmetric instability. Considering the fact that a neutral state ($PV_{\theta e} \approx 0$) for CSI is often observed in the real atmosphere, it may be worthwhile to design a new turbulence parameterization scheme which could result in the downgradient mixing of $PV_{\theta e}$.

APPENDIX

SPECIFICATION OF INITIAL M and θ

In the basic state, the along-band wind v_0 is specified to have a constant vertical shear but have no horizontal variation, that is

$$v_o = k_1 z + v_1 \qquad (A.1)$$

where $k_1 = 0.01\ s^{-1}$ and $v_1 = -45\ m\ s^{-1}$.

With a constant Coriolis parameter f (= $1 \times 10^{-4}\ s^{-1}$), the surfaces of initial absolute momentum M_0 will be straight lines in the cross-band section,

$$M_o = v_o + fx = k_1 z + fx + v_1 \qquad (A.2)$$

To get a dry symmetrically stable state, we set the dry potential vorticity to 0.3 pvu,

$$PV(t=0) = PV_o = 0.3\ pvu \qquad (A.3)$$

As a result, the surfaces of initial potential temperature θ_0 will also be straight lines in the cross-band section and can be calculated as follows.

First, we assume that θ_0 has the form

$$\theta_o = Ax + Bz + \theta_1 \qquad (A.4)$$

we obtain

$$A = \frac{\partial \theta_o}{\partial x}, \quad B = \frac{\partial \theta_o}{\partial z}, \quad \theta_1 = \theta_o(x=0, z=0) \qquad (A.5)$$

and we set $\theta_1 = 285$ K.

Secondly, using (A.1), (A.5) and thermal wind relation

$$\frac{\partial\theta_o}{\partial x} = \frac{f\theta_2}{g}\frac{\partial v}{\partial z} \quad , \tag{A.6}$$

where $\theta_2 = 320$ K and $g = 9.8$ m s^{-2}, we get

$$A = \frac{\partial\theta_o}{\partial x} = \frac{f\theta_2 k_1}{g} \tag{A.7}$$

Thirdly, using (A.2), (A.3) and (A.7), we get

$$B = \frac{\partial\theta_o}{\partial z} = \frac{1}{f}\left[PV_o + \frac{f\theta_2}{g}k_1^2\right] \tag{A.8}$$

Finally, substituting (A.7) and (A.8) into (A.4), we obtain

$$\theta_o = \left(\frac{f\theta_2 k_1}{g}\right)x + \left(\frac{PV_o}{f} + \frac{\theta_2 k_1^2}{g}\right)z + \theta_1 \tag{A.9}$$

REFERENCES

Bennetts, D. A., and B. J. Hoskins, 1979: Conditional symmetric instability — a possible explanation for frontal rainbands. *Quart. J. Roy. Meteor. Soc.*, 105, 945-962.

——, and J. C. Sharp, 1982: The relevance of conditional symmetric instability to the prediction of mesoscale frontal rainbands. *Quart. J. Roy. Meteor. Soc.*, 108, 595-602.

Bolton, D., 1980: The computation of equivalent potential temperature. *Mon. Wea. Rev.*, 108, 1046-1053.

Browning, K. A., M.E. Hardman, T. W. Harrold and C. W. Pardoe, 1973: The structure of rainbands within a mid-latitude depression. *Quart. J. Roy. Meteor. Soc.*, 99, 215-231

Byrd, G. P., 1989: A composite analysis of winter season overrunning precipitation bands over the southern plains of the United States. *J. Atmos. Sci.*, 46, 1119-1132.

Eliassen, A. and E. Kleinschmidt, 1957: Dynamic Meteorology. *Handb. Phys., Berlin*, 48, 71-72.

Emanuel, K. A., 1979: Inertial instability and mesoscale convective systems. Part 1: Linear theory of inertial instability in rotating viscous fluids. *J. Atmos. Sci.*, 36, 2425-2449.

——, 1983a: The Lagrangian parcel dynamics of moist symmetric instability. *J. Atmos. Sci.*, 40, 2368-2376.

——, 1983b: On assessing local conditional symmetric instability from atmospheric soundings. *Mon. Wea. Rev.*, 111, 2016-2033.

——, 1985: Frontal circulations in the presence of small moist symmetric stability. *J. Atmos. Sci.*, 42,1062-1071.

——, M. Fantini and A. J. Thorpe, 1987: Baroclinic Instability in an environment of small stability to slantwise moist convection. Part I: Two-dimensional models. *J. Atmos. Sci*, 44, 1559-1573.

——, 1988: Observational evidence of slantwise convective adjustment. *Mon. Wea. Rev.*, 116, 1805-1816.

Hane, C. E., 1986: Extratropical squall lines and rainbands, *Mesoscale Meteorology and Forecasting*. edited by Peter S. Ray, American Meteorological Society, 359-398.

Harlow, F. H., and J. E. Welch, 1965: Numerical calculation of time dependent viscous incompressible flow of fluid with free surface. *Phys. of Fluids*, 8, 2182-2189.

Hedley, M., and M. K. Yau, 1988: Radiation boundary conditions in numerical modelling. *Mon. Wea. Rev.*, 116, 1721-1736.

Hobbs, P. V., T. J. Matejka, P. H. Herzegh, J. D. Locatelli and R. A. Houze, Jr., 1980: The mesoscale and microscale structure and organization of clouds and precipitation in midlatitude cyclones. I: A case study of a cold front. *J. Atmos. Sci.*, 37, 568-596.

Hoskins, B. J., 1974: The role of potential vorticity in symmetric stability and instability. *Quart. J. Roy. Meteor. Soc.*, 100, 480-482.

——, 1978: Baroclinic instability and frontogenesis, *Rotating Fluid in Geophysics*, edited by P. H. Roberts and A. M. Soward, Academic Press, 171-203.

Houze, R. A., Jr. 1981: Structures of atmospheric precipitation systems: A global survey. *Radio Sci.*, 16, 671-689.

Knight, D. J. and P. V. Hobbs, 1988: The mesoscale and microscale structure and organization of clouds and precipitation in midlatitude cyclones. Part XV: A numerical modelling study of frontogenesis and cold-frontal rainbands. *J. Atmos. Sci.*, 45, 915-930.

Ogura, Y. and R. B. Wilhelmson, 1972: The pressure perturbation and the numerical modelling of a cloud. *J. Atmos. Sci.*, 29, 1295-1307.

Parsons, D. B. and P. V. Hobbs, 1983: The mesoscale and microscale structure and organization of clouds and precipitation in midlatitude cyclones. XI: Comparisons between observational and theoretical aspects of rainbands. *J. Atmos. Sci.*, 40, 2377-2397.

Persson, P. O. G. and T. T. Warner, 1991: Model generation of spurious gravity waves due to inconsistency of the vertical and horizontal resolution. *Mon. Wea. Rew.*, 119, 917-935

Reuter, G. W., and M. K. Yau, 1987a: Mixing mechanisms in cumulus congestus clouds. Part II: Numerical simulations. *J. Atmos. Sci.* 44, 798-827.

——, and ——, 1987b: Numerical modelling of cloud development in a sheared environment. *Contrib. Atmos. Phys.*, 60, 65-80.

——, and ——, 1990: Observations of slantwise convective instability in winter cyclones. *Mon. Wea. Rev.*, 118, 447-458.

Rogers, R. R., and M. K. Yau, 1989: *A Short Course in Cloud Physics.* 3rd Ed. Pergamon Press, Oxford, pp 293.

Saitoh, S., and H. Tanaka, 1987: Numerical experiments of conditional symmetric baroclinic instability as a possible cause for frontal rainband formation. Part I. A basic experiment. *J. Meteor. Soc. Japan*, 65, 675-708.

——, and ——, 1988: Numerical experiments of conditional symmetric baroclinic instability as a possible cause for frontal rainband formation. Part II. Effects of water vapor supply. *J. Meteor. Soc. Japan*, 66, 39-53.

Seltzer, M. A., R. E. Passarelli and K. A. Emanuel, 1985: The possible role of symmetric instability in the formation of precipitation bands. *J. Atmos. Sci.*, 42, 2207-2219.

Steiner, J. T., 1982: An axial symmetric cloud model: Development and simulations. Stormy Weather Group Scientific Report MW-94, McGill University, Montreal, pp 55.

Stone, P. H., 1966: On non-geostrophic baroclinic stability. *J. Atmos. Sci.*, 23, 390-400

Thorpe, A. J., and K. A. Emanuel, 1985: Frontogenesis in the presence of small stability to slantwise convection. *J. Atmos. Sci.*, 42, 1809-1842.

——, B. J. Hoskins and V. Innocentini, 1989: The parcel method in a baroclinic atmosphere. *J. Atmos. Sci.*, 46, 1274-1284.

——, and R. Rotunno, 1989: Nonlinear aspects of symmetric instability. *J. Atmos. Sci.*, 46, 1285-1299.